A novel inhibitor of the mitochondrial respiratory complex I with uncoupling properties exerts potent antitumor activity

Martine Cordier-Bussat

martine.cordier-bussat@lyon.unicancer.fr

CRCL

Alaa AL ASSI

Université Grenoble Alpes, Inserm U1055

Solène POSTY

Centre de Recherche en cancérologie de Lyon, INSERM U1052, CNRS 5286

Frédéric Lamarche

Univ Grenoble Alpes

Amel CHEBEL

Centre International de Recherche en Infectiologie (Team LIB)

Jérôme Guitton

Hospices Civils de Lyon

Renaud PRUDENT

Université Grenoble Alpes, Inserm U1209, CNRS UMR5309

Laurence LAFANECHERE

Université Grenoble Alpes, Inserm U1209, CNRS UMR5309

Stéphane GIRAUD

CRCL

Patrick DALLEMAGNE

Normandie Université, UNICAEN https://orcid.org/0000-0002-4845-615X

Peggy Suzanne

https://orcid.org/0000-0002-6080-8306

Laurent GENESTIER

Centre International de Recherche en Infectiologie

Marie Castets

INSERM U1052 https://orcid.org/0000-0002-6758-0017

Eric Fontaine

Univ Grenoble Alpes https://orcid.org/0000-0002-5204-9477

Marc Billaud

INSERM U1052

Article

Keywords:

Posted Date: July 18th, 2023

DOI: https://doi.org/10.21203/rs.3.rs-3144730/v1

Additional Declarations: (Not answered)

Version of Record: A version of this preprint was published at Cell Death & Disease on May 2nd, 2024.
See the published version at https://doi.org/10.1038/s41419-024-06668-9.

1

A novel inhibitor of the mitochondrial respiratory complex I with uncoupling properties exerts potent antitumor activity

Alaa Al Assi[1], Solène Posty[2], Frédéric Lamarche[1], Amel Chebel[3], Jérôme Guitton[4], Renaud Prudent[5], Laurence Lafanechère[5], Stéphane Giraud[6], Patrick Dallemagne[7], Peggy Suzanne[7], Laurent Genestier[3], Marie Castets[2], Eric Fontaine[1]*, Marc Billaud[2]* and Martine Cordier-Bussat[2]*

[1] Université Grenoble Alpes, Inserm U1055, Laboratoire de Bioénergétique Fondamentale et Appliquée (LBFA), Grenoble, France

[2] Cell death and Childhood Cancers Laboratory, Centre de Recherche en Cancérologie de Lyon (CRCL), INSERM U1052- CNRS UMR5286, Université Claude Bernard de Lyon1, Centre Léon Bérard, LabEx DEVweCAN, Institut Convergence Plascan, Lyon, France.

[3] Centre International de Recherche en Infectiologie (Team LIB), Equipe labellisée La Ligue 2017 and 2023. Université Lyon, INSERM, U1111, Université Claude Bernard Lyon 1, Centre National de la Recherche Scientifique, UMR5308, ENS de Lyon, Lyon, France.

[4] Laboratoire de biochimie et pharmacologie-toxicologie, Centre Hospitalier Lyon-Sud, Hospices Civils de Lyon, F-69495, Pierre Bénite, France. Laboratoire de Toxicologie, Faculté de pharmacie ISPBL, Université Lyon 1, F-69373, Lyon, France.

[5] Université Grenoble Alpes, Inserm U1209, CNRS UMR5309, Institute for Advanced Biosciences, Grenoble, France

[6] Center for Drug Discovery and Development, Synergie Lyon Cancer Foundation, Lyon, Cancer Research Center, Centre Léon Bérard, Lyon, France

[7] Normandie Univ., UNICAEN, CERMN, 14000 Caen, France

*Co-last authors and corresponding authors
martine.cordier-bussat@inserm.fr, Marc.BILLAUD@lyon.unicancer.fr, eric.fontaine@univ-grenoble-alpes.fr

Running title: A novel OXPHOS inhibitor with uncoupling properties

Conflict of interest statement: The authors declare no competing interests.

ABSTRACT

Cancer cells are highly reliant on bioenergetic processes to support their growth and survival. Disrupting these metabolic pathways, notably by targeting the electron transport chain complexes (ETC-I to V) in the mitochondrial bioenergetic hub, has become an attractive therapeutic strategy. As a result, the pursuit of identifying clinically effective new inhibitors of the respiratory chain with minimized adverse effects stands as a significant objective. Here, we characterize a first in class OXPHOS inhibitor compound called MS-L6, which behaves as an inhibitor of ETC-I, combining inhibition of NADH oxidation and decoupling effect. MS-L6 is effective on both intact and fragmented mitochondrial membranes, indicating that its efficacy does not rely on its accumulation within the mitochondria. MS-L6 reduces ATP synthesis and induces a metabolic shift with increased glucose consumption and lactate production in cancer cell lines, while having minimal effects on primary hepatocytes. Its dose-dependently inhibits cell proliferation or induces cell death in a wide range of cancer cell lines, including B-cell and T-cell lymphoma, as well as pediatric sarcoma. Furthermore, ectopic expression of *Saccharomyces cerevisiae* NADH-dehydrogenase NDI1 partially restores the viability of lymphoma B cells treated with MS-L6, demonstrating that inhibition of NADH oxidation is key for its antitumoral activity. Finally, MS-L6 administration induces a robust inhibition of lymphoma tumor growth in two murine xenograft models, without significant toxicity. Therefore, our data unveil MS-L6 as an inhibitor of oxidative phosphorylation (OXPHOS), with an unexpected dual mechanism of action on the respiratory chain. Additionally, MS-L6 demonstrates potent antitumoral properties in preclinical models, positioning it as the pioneering member of a promising new drug class to be assessed for cancer therapy.

INTRODUCTION

The transformation, development and spread of malignant cells generate and rely on metabolic plasticity[2-4]. The uncontrolled growth of cancer cells requires energy, stored in ATP molecules, notably produced by the mitochondrial respiratory chain (MRC) through oxidative phosphorylation mechanism (OXPHOS) which is often upregulated during the progression of a variety of adult and pediatric cancers[5], including hematological malignancies, such as lymphoma[6] and leukemia[7-9], but also other solid cancers[10] and sarcoma[11,12]. ATP production by mitochondria involves three steps[13]: i) the catabolism of carbohydrates, lipids and amino acids (AA) into NADH+H+ and $FADH_2$, CO_2 and NH_3 (when AA are catabolized) , ii) the oxidation of NADH+H+ and $FADH_2$ by the MRC (electron transport chain complexes ETC-I to IV) located in the inner mitochondrial membrane (IMM), resulting in an electron flux (the consumed oxygen acting as a terminal electron acceptor) and the expulsion of protons contributing to the generation of the proton gradient and iii) the consumption of the proton gradient by the ATPase leading to the synthesis of ATP from ADP and phosphate (Fig. S1)[14]. The measurement of the oxygen consumption rate (OCR) indirectly reflects OXPHOS activity of the cells[15]. Since cancer cells are dependent on this energy, targeting bioenergetic processes and biosynthetic pathways of mitochondria is a widely pursued strategy for the development of antitumoral drugs[5,16]. Several modulators of OXPHOS are described, acting as disruptors of either electron or proton transport. Among these are strong inhibitors that target ETC-1 and mitochondrial uncouplers, which are of particular interest and extensively studied. ETC-1 inhibitors (such as rotenone, metformin, IACS-010759, and IM156) inhibit NADH oxidation and electron transfer in MRC[17], while mitochondrial uncouplers (such as FCCP and BAM-15) mediate proton transport into the mitochondrial matrix via a pathway independent of ATP synthase and thus dissipate proton gradient[18]. They all reduce OXPHOS efficacy and yield of ATP production, but through distinct mechanisms. Mitochondrial uncouplers increase OCR, while classical ETC-1 inhibitors decrease OCR.

The clinical success of metformin, an anti-diabetic compound, first suggested the relevance of an anti-metabolic pharmacological approach in the treatment of cancer[19]. Indeed, epidemiological studies have shown that its widespread use reduces cancer incidence in diabetic patients[20,21], although the magnitude of this effect has been debated[22]. This observation has led to a strong interest in ETC-I inhibitors for cancer therapy. Clinical trials are underway to evaluate metformin and several other OXPHOS inhibitors effectiveness in preventing and treating various types of cancers[23]. Although compromising adverse side effects were observed for several of them[24], other molecules will be soon tested in advanced phases[25]. In this context, the identification of new inhibitors with novel mechanisms of action remains essential to effectively mitigate adverse side effects in new drugs candidates[26,27]. Here, we characterized a novel molecule, MS-L6, targeting OXPHOS with an unexpected mechanism of action. Succinctly, it has a dual effect: it inhibits NADH oxidation, while acting as an uncoupler. MS-L6 exhibits mild cytotoxic effects on various cancer cell lines and remarkably impedes tumor growth in preclinical mouse cancer models without toxicity. These results provide evidence for a new class of OXPHOS modulators with potential antitumor effects.

RESULTS

MS-L6 inhibits respiration through ETC-I

MS-L6 was previously described as a bis-thioureidic synthetic derivative with anti-amoebic properties[28,29] and emerged following a chemical library screen to identify new compounds that could induce cell death and interfere with metabolic pathways. Regarding its chemical structure, it is distantly related to diguanidine compounds, such as metformin and phenformin ETC-I inhibitors[30]. Hence, we initially tested by oxygraphy the effects of MS-L6 on the OCR of freshly isolated rat hepatocytes and of two lymphoma cell lines, namely RL and K422, upon titration with increasing concentrations. MS-L6 dose dependently decreased the OCR of the 3 cell types (Fig.1A). The IC_{50} of MS-L6 was five-fold higher in hepatocytes than in cancer cells,

suggesting that the latter cells have a stronger sensitivity to the molecule. Complete OCR inhibition was observed in all cases at 50µM, which we then used to dissect the effects of MS-L6 on mitochondria.

To determine at which level along the MRC MS-L6 acted, we examined its effects on 2% digitonin-permeabilized cells. Digitonin treatment at low concentrations removes cholesterol from plasma membranes and thus directly exposes mitochondria to extracellular metabolic substrates added to the experimental buffer. Under ADP phosphorylating conditions (state 3/ATP synthase is active), MS-L6 significantly decreased the OCR of permeabilized hepatocytes, RL and K422 cells in the presence of ETC-I substrate (glutamate/malate), but not significantly in the presence of ETC-II substrate (succinate) and rotenone, highlighting its affinity for ETC-I (Fig.1B).

Under non-phosphorylating conditions (state 4/ resting OXPHOS), *i.e.,* in the presence of oligomycin that inhibits ATP synthase, MS-L6 reduced residual glutamate/malate-driven OCR (ETC-I-dependent) and unexpectedly increased succinate/rotenone-driven OCR (ETC-I-independent) in a concentration-dependent manner in all cells tested (Fig.1C). These findings suggest that MS-L6 also acts as an uncoupler of OXPHOS, typically by inducing a process that consumes oxygen without leading to ATP synthesis.

We next tested whether MS-L6-induced inhibition of ETC-I was dependent on the integrity of the mitochondrial membrane potential ΔΨm. Since mitochondrial fragments lack ΔΨm, we compared ETC-I-driven OCR of intact mitochondria to fragmented mitochondria stimulated with glutamate/malate and NADH, respectively. MS-L6 decreased the OCR of both intact and fragmented mitochondria with similar IC_{50} values (Fig.1D, E), indicating that MS-L6 inhibited ETC-I-driven OCR regardless of mitochondrial membrane integrity, ΔΨm maintenance or matrix accumulation.

To confirm that ETC-I was the target of MS-L6, we evaluated the effects of MS-L6 on the OCR of mitochondrial fragments specifically powered through ETC-I, -II, and -IV using

NADH, succinate and TMPD/ascorbate substrates, respectively. Once again, MS-L6 exclusively inhibited OCR through ETC-I (Fig.1F). Finally, we measured NADH oxidation by ETC-I that was functionally isolated from remaining part of MRC by incubating mitochondrial fragments with NADH substrate in the presence of KCN to block electron transfer through complex IV. Decylubiquinone was then added as an ultimate acceptor of electrons resulting from NADH oxidation. In these conditions, MS-L6 completely blocked NADH oxidation (Fig.1I). Furthermore, we constructed Michaelis-Menten saturation curves showing the OCR of mitochondrial fragments incubated with either DMSO or MS-L6, upon titration with increasing concentrations of NADH. The maximal OCR (Vmax) and NADH concentrations at half-maximal OCR (Km) decreased in the presence of MS-L6, suggesting that MS-L6 inhibited ETC-I without competing with NADH (Fig.1H).

MS-L6 acts on ΔΨm.

Our findings that MS-L6 increased succinate/rotenone-driven OCR in Fig.1C led us to hypothesize that MS-L6 may be endowed with uncoupling properties. We thus evaluated its effect on ΔΨm. In intact freshly isolated rat liver mitochondria energized with ETC-I substrate, MS-L6 greatly reduced ΔΨm (Fig.2A). Interestingly, when incubated with rotenone, an ETC-I inhibitor lacking uncoupling properties at a dose that completely inhibits OCR, only a slight decrease in ΔΨm was observed. The subsequent addition of the protonophore uncoupler FCCP completely depolarized ΔΨm. The residual ΔΨm following the addition of rotenone was higher than that observed with MS-L6, indicating that MS-L6 alone induced a stronger depolarization than rotenone, and confirmed that it has uncoupling properties. MS-L6 caused a minor yet perceptible decrease in ΔΨm when the ETC-II substrate was present, whereas rotenone had no effect (Fig.2B). As anticipated, FCCP entirely depleted ΔΨm (Fig.2B). Of note, pre-incubation with the permeability transition pore (PTP) inhibitor, cyclosporin A, did not attenuate MS-L6

effect in the presence of ETC-I substrate, suggesting that it was not mediated through the PTP opening (Fig.2C).

The ATP synthase, also referred to as ECT-V, uses the free energy of the electrochemical gradient of protons generated by the MRC to synthesize ATP. ATP synthase is a reversible proton pump that can also hydrolyze ATP to restore ΔΨm. We questioned whether the uncoupling effect of MS-L6 could be compensated for by reversing the activity of ATP synthase. This "ATP hydrolyzing" activity of ATP synthase was turn on by the addition of ATP following either MS-L6 or FCCP induced depolarization, to intact mitochondria energized with ETC-I substrate. The addition of ATP restored ΔΨm following MS-L6 treatment (Fig.2D) but not FCCP treatment (Fig.2E). To further ascertain that ATP-induced compensation of ΔΨm was mediated via ATP synthase, we then added ATP in combination with oligomycin, an irreversible inhibitor of ATP synthase. A very slight restoration of ΔΨm was observed in these conditions, confirming that ATP hydrolysis by ATP synthase compensated for MS-L6-induced depolarization (Fig.2F). Next, we measured the effects of MS-L6 on the ΔΨm in intact cancer cells. Compared to untreated cells, MS-L6 decreased ΔΨm, by at least twice as much as rotenone, in both RL and K422 cells (Fig.2G, H). Knowing that oligomycin alone had no significant effect on ΔΨm, the co-treatment of cancer cells with MS-L6 and oligomycin resulted in a greater decrease in ΔΨm than treatment with MS-L6 alone. Similar trends were observed upon cotreatment with rotenone and oligomycin.

Taken together, these results confirm that MS-L6, in addition to inhibiting ETC-I, also has an uncoupling effect that induces ATP consumption to restore ΔΨm.

MS-L6 modifies the energy status in cancer cells.

Next, we studied the consequences of MS-L6 treatment on cellular energy status. The total cellular adenine nucleotide content was measured using HPLC, resulting in chromatograms showing the respective ATP, ADP and AMP peaks (Fig.3A). The ATP/ADP ratios were

198 calculated and are shown in Fig.3B. Hepatocytes treated with 50µM MS-L6 had ATP/ADP
199 ratios similar to those of untreated cells, irrespective of treatment duration. Conversely, MS-
200 L6 treatment drastically decreased the ATP/ADP ratios in RL and K422 cells, especially during
201 the first few hours of treatment. As MS-L6 administered at a dose that completely inhibited
202 OCR in all cell types collapsed the ATP/ADP ratio exclusively in cancer cells, we questioned
203 its stability/half-life in the culture medium of each cell type at early and late time points after
204 treatment. We collected these media at different time points and tested their effects on the
205 NADH-driven OCR of mitochondrial fragments. Media collected as early as 3 h post-treatment
206 of hepatocytes with MS-L6 had a very small inhibitory effect on the OCR (Fig.3C). Notably,
207 this inhibition was absent in the following hours, suggesting that MS-L6 was completely
208 metabolized by hepatocytes. Conversely, media collected at 6 and 24 h post-treatment of either
209 RL or K422 cells with MS-L6 strongly inhibited NADH-driven OCR of mitochondrial
210 fragments (Fig.3C).
211 Hence, unlike hepatocytes which normalize their energy status by rapidly detoxifying MS-L6,
212 cancer cells lack this ability and maintain functional MS-L6 levels, which result in cellular
213 energy collapse.
214
215 **MS-L6 induces a glycolytic shift in cancer cells.**
216 Inhibition of OXPHOS often induces a metabolic shift towards glycolysis, *i.e.,* increased
217 cellular glucose consumption and lactate production. As these two parameters were enhanced
218 in RL and K422 cells after 24 h treatment with MS-L6 (Fig.4A), we concluded that it induces
219 a glycolytic shift in these cells. No effect was observed on hepatocytes as expected.
220 We then compared the real-time metabolic effects of MS-L6 with those of other ECT-I
221 inhibitors using the Seahorse technology (Fig.4B). OCR and ECAR (extracellular acidification
222 rate, an indirect indicator of lactate production and glycolytic shift) were simultaneously
223 measured in RL and K422 cells treated with increasing concentration of MS-L6 (0.65 to 5µM)

for 100 min and compared with those of IACS-010759 and rotenone ETC-1 inhibitors used at the final concentrations (0.65 to 5µM) and (1 to 5nM), respectively. IACS-010759, similarly to rotenone, induced a strong and instantaneous inhibition of basal OCR in RL and K422 cells (upper panel). Comparatively, MS-L6 exerted a progressive and mild inhibition of OCR. Accordingly, the glycolytic shift visualised by ECAR increased immediately following IACS-010759 or rotenone treatment, albeit progressively and to a lesser extent after MS-L6 treatment (bottom panel).

Thus, the metabolic response elicited by MS-L6 differed significantly from that produced by IACS-010759 or rotenone, highlighting distinct mechanisms of action.

MS-L6 is cytostatic/cytotoxic to tumour cells.

We evaluated MS-L6 toxicity by measuring its real-time effect on the number of viable cells (Fig.5A). Since it is common that 50 to 70% of hepatocytes in primary cultures progressively die as they lose their phenotypic and metabolic features, we concluded that MS-L6 did not affect the viability of hepatocytes, in line with our previous observation that they metabolize MS-L6. On the contrary, 50µM MS-L6 completely stopped the proliferation of RL (the number of live cells at T0 remained unchanged over time) and killed K422 cells (the number of live cells decreased over time). Accordingly, flow cytometric analysis revealed mild and extensive death, highlighted by annexin V/PI co-labeling of RL and K422 cells, respectively, in response to treatment (Fig.S2).

We then compared the effects of MS-L6 with those of IACS-010759 and rotenone on a panel of human cell lines. In the screening of drug candidates, the concentration 10µM is conventionally considered as an upper limit[31]. We therefore chose to evaluate the cytotoxicity of MS-L6 at this concentration, knowing that 5µM was effective in inducing OCR and ECAR shifts in the previous experiments (Fig.4). Live and dead cells were quantified using automated flow cytometry, firstly in RL, K422 and SUDHL4 cells. In all cases, the number of live cells

decreased significantly 48h post-treatment with MS-L6, albeit to a lesser extent than that with IACS-010759 and rotenone (Fig.5B). Annexin V/PI labelling demonstrated that MS-L6 induced moderate cell death exclusively in K422 cells, while IACS-010759 and rotenone killed all three cell lines (Fig.5C). The large-scale analysis confirmed this decrease in the number of living cells, sometimes moderate and sometimes comparable to that of IACS-010759, for all the hematological cell lines analyzed (Fig.5D). The IC_{50} analysis using protease-based detection of live cells corroborated these observations (Fig.S3). This effect of MS-L6 was also observed in several solid tumor cell lines, especially in the pediatric rhabdomyosarcoma cell lines RH30 and RD (Fig.S4). Real-time imaging using fluorescent dyes confirmed that MS-L6 is (i) mostly cytostatic at a mild dose (10µM): fewer but viable cells are highlighted by green labeling and (ii) mostly cytotoxic at a high dose (50µM): most remaining cells are dead, highlighted by red labeling (Fig.S4).

NDI-1 complementation partially rescues cell viability after MS-L6 treatment.

To ascertain whether MS-L6 inhibition of ETC-I was responsible for its cytotoxicity in cancer cells, we performed complementation experiments with the *Saccharomyces cerevisiae* NDI-1 protein. NDI-1 oxidizes NADH in a similar way to the multi-subunit mammalian ETC-I but without pumping protons into the intermembrane space[32,33]. Interestingly, NDI-1 is resistant to most ETC-I inhibitors described in the literature. We first verified that NDI-1 was resistant to MS-L6 treatment. We functionally isolated NDI-1 from yeast mitochondria as in Figure 1I and we observed that the addition of MS-L6 did not block NADH oxidation in these conditions (Fig.6A), indicating that electron transfer through NDI-1 was not inhibited by MS-L6 and that NDI-1 could be used to complement ETC-I activity.

We then stably expressed the NDI-1 protein in K422 cells, using lentiviral vectors (Fig.S6). We evaluated the effect of MS-L6 treatment on these cells compared to their counterparts (without NDI-1 expression). IACS-010759 and rotenone were used as ETC-I inhibitor controls.

As expected, NDI-1 expression restored viability of K422 cells treated with IACS-010759 or rotenone (Fig.6B). A similar effect, although to a lesser extent, was observed in response to increasing doses of MS-L6, indicating that inhibition of ETC-I did contribute to K422 cell death.

MS-L6 displays antitumoral activity in a preclinical murine model.

Next, we evaluated the antitumoral activity of MS-L6 in preclinical SCID mice models. Pilot experiments were performed to address MS-L6 toxicity upon chronic intraperitoneal injections, 5 days per week, for 4 weeks, and with increasing concentrations from 10mg/kg to 50mg/kg. Mice showed no signs of toxicity under any of these conditions. LC/MS analysis performed in parallel allowed the dosage of the molecule in the sera of animals, which was correlated with the injected quantities (Fig.7A left). Then, subcutaneous xenografts of RL and SUDHL4 cells were performed to evaluate the effect of MS-L6 treatment on tumor growth (Fig.7A right). Remarkably, MS-L6 treatment at the dose of 50mg/kg induced a significant reduction in the volume of RL tumors and blocked the growth of SUDHL4 tumors, thus providing evidence of the antitumoral properties of the MS-L6 molecule in these pre-clinical models.

DISCUSSION

The characterization of MS-L6 reveals a novel inhibitor of the ETC-1 with uncoupling properties, that exerts potent antitumor activity. MS-L6 displays original characteristics that suggest that it acts through different targets and mechanisms of action when compared with other known inhibitors.

MS-L6 is an OXPHOS inhibitor that exhibits a moderate reduction in the OCR when compared to rotenone or IACS-010759. This mild effect is likely attributed to two cumulative and opposing mechanisms. Firstly, the inhibition of NADH oxidation decreases electron transfer along the MRC leading to OCR inhibition. Secondly, the decrease in the proton gradient,

associated with its uncoupling capacity, increases OCR. Additionally, this uncoupling effect is reversible and compensated for by ATP hydrolysis. ETC-1 consists of 45 protein subunits organized into four functional modules, which ensure both electron transfer and proton pumping[34]. By targeting one or more of these proteins, it is thus conceivable that MS-L6 cumulates two effects. However, the possibility of nonspecific protonophore activity cannot be ruled out. The ΔΨm is determined by the balance between the processes that generate and consume the proton gradient to regulate OXPHOS and the ATP yield. Two main processes can reduce the yield of OXPHOS: i) fewer protons are expelled per unit of oxygen consumed, for example when the MRC is fed downstream of ETC-I and NADH oxidation is inhibited and ii) proton re-entry is not coupled to ATP synthesis. Depending on the mechanism involved and its intensity, the consequences on ΔΨm and on OCR are variable. When these losses in yield are compensated for by an increase in MRC activity, the result is a weak (or no) ΔΨm drop with a concomitant increase in OCR. Otherwise, ΔΨm diminishes and may even be lost completely[35]. These processes explain the effects of MS-L6 on ΔΨm. When mitochondria are energized with ETC-II substrates, MS-L6 results in a low ΔΨm drop because the MRC compensates for proton re-entry. Conversely, when mitochondria are energized with ETC-I substrates, MS-L6 induces a strong ΔΨm drop due to the inhibition of ETC-I since the MRC cannot compensate for proton re-entry. Thus, MS-L6 behaves as a stronger ETC-I inhibitor than as an uncoupler. Ectopic expression of yeast NDI1 in K422 cells confirms its dual activity and demonstrates that ETC-I inhibition is central to its anti-proliferative effects. NDI1 is not a proton pump, and it only catalyzes electron transfer from NADH to the ubiquinone pool, without pumping protons from the matrix to the IMS[36]. However, by bypassing the inhibition of complex I, the expression of NDI1 allows the downstream complexes to function (oxygen consumption and production of the proton gradient). Accordingly, NDI1 restores cell growth almost completely in the presence of IACS-010759 or rotenone, but only partially with MS-L6. The combination of these two effects leads to a significant reduction in energy levels, as measured by the ATP to ADP ratio,

despite an increase in glycolysis. The dual stress caused by MS-L6 necessitates double compensation that might contribute to its antitumoral properties. ETC-I inhibition constrains cancer cells to rely on "aerobic glycolysis" while uncoupling consumes much of the ATP generated through aerobic glycolysis. Cancer cells can survive ETC-I inhibition if they are able to maintain $\Delta\Psi m$[4], by reversing the activity of ATP synthase.

MS-L6 is non-toxic to native hepatocytes unlike cancer cells. Hepatocytes have a strong and fast ability to metabolize it since supernatants of MS-L6-treated hepatocytes lose the ability to inhibit ETC-1, unlike tumour cells. Accordingly, it is well-tolerated in a murine preclinical model. Non-tumoral cells may be able to compensate for the metabolic stress induced by MS-L6 treatment, although the underlying mechanisms remain to be explained. Various uncouplers are more effective against cancer cells than normal cells[37]. Consequently, several such compounds are being tested in clinical trials for cancer treatment, although none have yet been approved for clinical use[37]. The uncoupling properties of MS-L6 may partially account for its selective effects on tumor cells and potentiate its antitumor properties. Moreover, the metabolic stress induced in the tumor cells may serve as an initiator of a pro-inflammatory response sustaining the antitumoral efficacy of MS-L6 in preclinical models [38].

There is a growing interest in using OXPHOS inhibitors to treat cancer. However, the highly potent ETC-I inhibitors may have adverse effects that could obstruct their clinical use. Phenformin was withdrawn from the market due to a higher risk of lactic acidosis[39]. Very recently, a phase 1 clinical trial for IACS-01759 showed limited antitumor activity linked to high levels of blood lactate and peripheral neuropathy[24]. A promising first-in-human study of IM-156, a metformin analog, revealed a favorable safety profile and tolerability at the recommended phase 2 dose[25]. Enhancing the antitumoral efficacy of MS-L6 may require combining it with inhibitors that target not only metabolic properties of tumour cells but also different cell pathways, including those of non-cancer stromal and immune cells in the microenvironment. This approach deserves further exploration. Our study provides a proof-of-

concept that a novel class of molecules with a dual activity, exemplified by MS-L6, could become effective chemotherapeutic drugs against tumours.

ACKNOWLEDGEMENTS

The authors acknowledge the AniRA-ImmOs metabolic phenotyping facility, the animal housing facility, the cytometry platform (SFR Biosciences UAR3444/CNRS, US8/Inserm, ENS de Lyon, UCBL). We gratefully thank Laurence Canaple for precious technical assistance during Seahorse experiments realization.

The authors express their gratitude to Nathalie Bissay for technical assistance, and all the staff of the LG and MC laboratory team for their excellent suggestions and valuable technical support. They thank Laetitia Martin for managing the IC_{50} experiments and analyzing the associated data. The authors express their gratitude to Dr Anne Devin (IBCG CNRS, Bordeaux, France) for the precious gift of Yeast mitochondria. The authors are grateful to Brigitte Manship (CRCL, Lyon) for editing this paper.

The authors are grateful to all their financial supports : DEV2CAN, Institut Convergence Plascan, Ligue Nationale contre le Cancer, Ligne de Haute-Savoie, CLARA, INSERM, CNRS, SATT PULSALYS and Fonds Agir pour les maladies Chroniques.

AUTHOR CONTRIBUTION STATEMENT

AAA performed in vitro experiments related to mitochondria, analyzed data, wrote results and M&M and prepared corresponding paragraphs and figures. SP performed in vitro experiments related to cytotoxic effects, analyzed data and prepared corresponding figures. FL performed complementary experiments related to mitochondria. AC performed part of in vivo experiments. JG performed LC/MS analysis of mouse blood, analyzed the data. RP performed chemical screening experiments. LL supervised chemical screening experiments. SG

supervised IC_{50} experiments, provide project expertise. PD provided chemical expertise. PZ synthesized MS-L6 molecule, provided chemical input. LG provided technical advice and scientific input. MC provided scientific expertise and critically read the paper.

EF discussed and conducted the study on mitochondria and wrote the manuscript and grants applications. MB conceived the study, discussed the project, and wrote the manuscript and grants applications. MCB co-conceived the project, conducted the study, performed in vitro experiments on the Seahorse, wrote the paper and grants applications.

The paper has been read and approved by all named authors.

FUNDING STATEMENT

This work was supported by the grants from the following funders:

Ligue nationale contre le Cancer to MB,

CLARA (Oncostarter program 2016) to MB and MCB,

CNRS (Pre maturation program 2019) to MB and MCB

SATT PULSALYS (maturation program 2021)

ANR-17-CONV-0002 PLASCAN to MB and MCB

Fonds Agir pour les maladies Chroniques to EF

AAA was supported by a fellowship from « ministère de l'enseignement supérieur et de la recherche français ».

DATA AVAILABILITY STATEMENT

All data generated or analyzed during this study are available from the corresponding author on reasonable request.

REFERENCES

1 DeBerardinis, R. J. & Chandel, N. S. We need to talk about the Warburg effect. *Nat Metab* **2**, 127-129 (2020). https://doi.org:10.1038/s42255-020-0172-2

2 DeBerardinis, R. J. & Chandel, N. S. Fundamentals of cancer metabolism. *Sci Adv* **2**, e1600200 (2016). https://doi.org:10.1126/sciadv.1600200

3 Vyas, S., Zaganjor, E. & Haigis, M. C. Mitochondria and Cancer. *Cell* **166**, 555-566 (2016). https://doi.org:10.1016/j.cell.2016.07.002

4 Martinez-Reyes, I. & Chandel, N. S. Cancer metabolism: looking forward. *Nat Rev Cancer* **21**, 669-680 (2021). https://doi.org:10.1038/s41568-021-00378-6

5 Sica, V., Bravo-San Pedro, J. M., Stoll, G. & Kroemer, G. Oxidative phosphorylation as a potential therapeutic target for cancer therapy. *Int J Cancer* **146**, 10-17 (2020). https://doi.org:10.1002/ijc.32616

6 Kluckova, K., D'Avola, A. & Riches, J. C. Advances in Understanding of Metabolism of B-Cell Lymphoma: Implications for Therapy. *Cancers (Basel)* **14** (2022). https://doi.org:10.3390/cancers14225552

7 de Beauchamp, L., Himonas, E. & Helgason, G. V. Mitochondrial metabolism as a potential therapeutic target in myeloid leukaemia. *Leukemia* **36**, 1-12 (2022). https://doi.org:10.1038/s41375-021-01416-w

8 Madhusoodhan, P. P., Carroll, W. L. & Bhatla, T. Progress and Prospects in Pediatric Leukemia. *Current Problems in Pediatric and Adolescent Health Care* **46**, 229-241 (2016). https://doi.org:https://doi.org/10.1016/j.cppeds.2016.04.003

9 Bosc, C., Selak, M. A. & Sarry, J. E. Resistance Is Futile: Targeting Mitochondrial Energetics and Metabolism to Overcome Drug Resistance in Cancer Treatment. *Cell Metab* **26**, 705-707 (2017). https://doi.org:10.1016/j.cmet.2017.10.013

10 Zuzcak, M. & Trnka, J. Cellular metabolism in pancreatic cancer as a tool for prognosis and treatment (Review). *Int J Oncol* **61** (2022). https://doi.org:10.3892/ijo.2022.5383

11 Vial, J. *et al.* Low expression of ANT1 confers oncogenic properties to rhabdomyosarcoma tumor cells by modulating metabolism and death pathways. *Cell Death Discov* **6**, 64 (2020). https://doi.org:10.1038/s41420-020-00302-1

12 Chen, X. *et al.* Targeting oxidative stress in embryonal rhabdomyosarcoma. *Cancer Cell* **24**, 710-724 (2013). https://doi.org:10.1016/j.ccr.2013.11.002

13 Bonora, M. *et al.* ATP synthesis and storage. *Purinergic Signal* **8**, 343-357 (2012). https://doi.org:10.1007/s11302-012-9305-8

14 Guan, S., Zhao, L. & Peng, R. Mitochondrial Respiratory Chain Supercomplexes: From Structure to Function. *Int J Mol Sci* **23** (2022). https://doi.org:10.3390/ijms232213880

15 Divakaruni, A. S. & Jastroch, M. A practical guide for the analysis, standardization and interpretation of oxygen consumption measurements. *Nat Metab* **4**, 978-994 (2022). https://doi.org:10.1038/s42255-022-00619-4

16 Stine, Z. E., Schug, Z. T., Salvino, J. M. & Dang, C. V. Targeting cancer metabolism in the era of precision oncology. *Nat Rev Drug Discov* **21**, 141-162 (2022). https://doi.org:10.1038/s41573-021-00339-6

17 Ashton, T. M., McKenna, W. G., Kunz-Schughart, L. A. & Higgins, G. S. Oxidative Phosphorylation as an Emerging Target in Cancer Therapy. *Clin Cancer Res* **24**, 2482-2490 (2018). https://doi.org:10.1158/1078-0432.CCR-17-3070

18 Demine, S., Renard, P. & Arnould, T. Mitochondrial Uncoupling: A Key Controller of Biological Processes in Physiology and Diseases. *Cells* **8** (2019). https://doi.org:10.3390/cells8080795

19 Currie, C. J., Poole, C. D. & Gale, E. A. The influence of glucose-lowering therapies on cancer risk in type 2 diabetes. *Diabetologia* **52**, 1766-1777 (2009). https://doi.org:10.1007/s00125-009-1440-6

20 Franciosi, M. *et al.* Metformin therapy and risk of cancer in patients with type 2 diabetes: systematic review. *PLoS One* **8**, e71583 (2013). https://doi.org:10.1371/journal.pone.0071583

21 Noto, H., Goto, A., Tsujimoto, T. & Noda, M. Cancer risk in diabetic patients treated with metformin: a systematic review and meta-analysis. *PLoS One* **7**, e33411 (2012). https://doi.org:10.1371/journal.pone.0033411

22 Lord, S. R. & Harris, A. L. Is it still worth pursuing the repurposing of metformin as a cancer therapeutic? *Br J Cancer* **128**, 958-966 (2023). https://doi.org:10.1038/s41416-023-02204-2

23 Greene, J., Segaran, A. & Lord, S. Targeting OXPHOS and the electron transport chain in cancer; Molecular and therapeutic implications. *Semin Cancer Biol* **86**, 851-859 (2022). https://doi.org:10.1016/j.semcancer.2022.02.002

24 Yap, T. A. *et al.* Complex I inhibitor of oxidative phosphorylation in advanced solid tumors and acute myeloid leukemia: phase I trials. *Nat Med* **29**, 115-126 (2023). https://doi.org:10.1038/s41591-022-02103-8

25 Janku, F. *et al.* First-in-human study of IM156, a novel potent biguanide oxidative phosphorylation (OXPHOS) inhibitor, in patients with advanced solid tumors. *Invest New Drugs* **40**, 1001-1010 (2022). https://doi.org:10.1007/s10637-022-01277-9

26 Bian, C. *et al.* Targeting Mitochondrial Metabolism to Reverse Radioresistance: An Alternative to Glucose Metabolism. *Antioxidants (Basel)* **11** (2022). https://doi.org:10.3390/antiox11112202

27 Zhao, Z., Mei, Y., Wang, Z. & He, W. The Effect of Oxidative Phosphorylation on Cancer Drug Resistance. *Cancers (Basel)* **15** (2022). https://doi.org:10.3390/cancers15010062

28 Saturnino, C., Buonerba, M., Paesano, N., Lancelot, J. C. & De Martino, G. In vitro anti-acanthamoeba action by thioureidic derivatives. *Farmaco* **58**, 819-822 (2003). https://doi.org:10.1016/S0014-827X(03)00138-1

29 Saturnino, C. *et al.* Antioxidant activity of thioureidic derivatives I. *Farmaco* **58**, 823-828 (2003). https://doi.org:10.1016/S0014-827X(03)00139-3

30 Foretz, M. & Viollet, B. [New promises for metformin: advances in the understanding of its mechanisms of action]. *Med Sci (Paris)* **30**, 82-92 (2014). https://doi.org:10.1051/medsci/20143001018

31 Shoemaker, R. H. The NCI60 human tumour cell line anticancer drug screen. *Nat Rev Cancer* **6**, 813-823 (2006). https://doi.org:10.1038/nrc1951

32 Wirth, C., Brandt, U., Hunte, C. & Zickermann, V. Structure and function of mitochondrial complex I. *Biochim Biophys Acta* **1857**, 902-914 (2016). https://doi.org:10.1016/j.bbabio.2016.02.013

33 Seo, B. B. *et al.* Molecular remedy of complex I defects: rotenone-insensitive internal NADH-quinone oxidoreductase of Saccharomyces cerevisiae mitochondria restores the NADH oxidase activity of complex I-deficient mammalian cells. *Proc Natl Acad Sci U S A* **95**, 9167-9171 (1998). https://doi.org:10.1073/pnas.95.16.9167

34 Giachin, G., Bouverot, R., Acajjaoui, S., Pantalone, S. & Soler-Lopez, M. Dynamics of Human Mitochondrial Complex I Assembly: Implications for Neurodegenerative Diseases. *Front Mol Biosci* **3**, 43 (2016). https://doi.org:10.3389/fmolb.2016.00043

35 Sibille, B. *et al.* The mitochondrial consequences of uncoupling intact cells depend on the nature of the exogenous substrate. *Biochem J* **355**, 231-235 (2001). https://doi.org:10.1042/0264-6021:3550231

36 Melo, A. M., Bandeiras, T. M. & Teixeira, M. New insights into type II NAD(P)H:quinone oxidoreductases. *Microbiol Mol Biol Rev* **68**, 603-616 (2004). https://doi.org:10.1128/MMBR.68.4.603-616.2004

37 Shrestha, R., Johnson, E. & Byrne, F. L. Exploring the therapeutic potential of mitochondrial uncouplers in cancer. *Mol Metab* **51**, 101222 (2021). https://doi.org:10.1016/j.molmet.2021.101222

38 Puschel, F. *et al.* Starvation and antimetabolic therapy promote cytokine release and recruitment of immune cells. *Proc Natl Acad Sci U S A* **117**, 9932-9941 (2020). https://doi.org:10.1073/pnas.1913707117
39 Kolata, G. B. The phenformin ban: is the drug an imminent hazard? *Science* **203**, 1094-1096 (1979). https://doi.org:10.1126/science.424735
40 Berry, M. N. & Friend, D. S. High-yield preparation of isolated rat liver parenchymal cells: a biochemical and fine structural study. *J Cell Biol* **43**, 506-520 (1969). https://doi.org:10.1083/jcb.43.3.506
41 Groen, A. K., Sips, H. J., Vervoorn, R. C. & Tager, J. M. Intracellular compartmentation and control of alanine metabolism in rat liver parenchymal cells. *Eur J Biochem* **122**, 87-93 (1982). https://doi.org:10.1111/j.1432-1033.1982.tb05851.x
42 Klingenberg, M. & Slenczka, W. [Pyridine nucleotide in liver mitochondria. An analysis of their redox relationships]. *Biochem Z* **331**, 486-517 (1959).

MATERIALS AND METHODS

Chemical compounds

MS-L6 was previously described [28,29] and provided by CERMN (Caen, France). The chemical compounds and kit assays are described in the complementary materials file (sup data).

Cell culture

The two human non-Hodgkin's B cell lymphoma cancer cell lines, RL (CVCL_1660) and Karpas422 here named K422 (CVCL_1325), were grown in RPMI 1640 medium GlutaMAX™ supplemented with 10% fetal bovine serum (FBS) and 1% penicillin-streptomycin. All other human cell lines are described in complementary materials file (sup data) and were maintained under the same culture conditions. Cell line authentication was performed using PCR assays that targeted short tandem repeat (STR) markers in DNA as fingerprints. Absence of mycoplasma was routinely detected.

Hepatocytes were isolated from Wistar rats according to the method of Berry and Friend[40] and modified by Groen et al.[41]. Hepatocytes were seeded onto PB-60 dishes in a mixture containing 66% DMEM 4.5 g/L glucose (Pan Biotech) and 22% M199 medium supplemented with 10%

FBS, 2mM glutamine, 1% penicillin-streptomycin and 0.2mg/mL fatty acid-free bovine serum albumin (BSA-FAF, Dutscher). Cells were maintained in a humidified incubator (37°C-5% CO_2).

Generation of NDI-overexpressing cells: Plasmids pLV[Exp]-EGFP:T2A:Puro-EF1A>sce_NDI1, pLV[Exp]-EGFP:T2A:Puro-EF1A>sce_mCherry and titered lentiviral particles were purchased from VectorBuilder. K422 lymphoma cells were transduced using a spinoculation protocol. Briefly, 1 x 10^6 cells were resuspended in fresh RPMI medium in a 6-well plate before adding 3 MOI of p_NDI1 or p_mCherry lentiviral particles per well. Plates were centrifugated at 1,000 *g* for 1 h at 32°C, then incubated at 37°C/5%CO2. On day 3 after transduction, 1µg/mL puromycin was added to the medium to select the transduced cells only.

Isolation of mitochondria from rat livers and preparation of mitochondrial fragments

Mitochondria were isolated from livers of Wistar rats through differential centrifugation in a medium containing 250mM sucrose, 25mM Tris-HCl and 1mM EGTA as previously described[42]. Mitochondrial fragments were prepared by breaking up mitochondrial membranes by exposing isolated mitochondria to repeated freeze/thaw cycles and subsequent incubation in ultrapure water (hypoosmotic shock). Mitochondrial breakdown was evidenced by the huge increase in oxygen consumption upon addition of NADH to mitochondrial fragments.

Measurement of oxygen consumption rates

The oxygen consumption rate (OCR) was measured using the MT200 respirometer cell (Strathkelvin Instruments): a thermostatically controlled respiratory chamber equipped with a Clark oxygen electrode and a magnetic stirrer to ensure continuous mixing of all components. All measurements were performed at 30°C.

Measurement of OCR of intact and permeabilized cells: To determine the immediate effect of MS-L6 on cellular respiration, the OCR of 5 x 10^6 RL, 5 x 10^6 K422 and 0.5 x 10^6 freshly

562 isolated rat hepatocytes was measured upon titration with an increasing concentration of MS-
563 L6. These cells were either suspended in 500µL of complete RPMI medium for OCR
564 measurements in intact cells or 500µL of mitochondrial assay buffer (125mM KCl, 1mM
565 EGTA, 20mM Tris, pH 7.4) for OCR measurements in permeabilized cells. In the first step,
566 cell suspensions were placed in the respirometry chamber. For OCR measurements in intact
567 cells, the respiratory chamber was directly sealed with a cap and recording of OCR was
568 immediately initiated. For permeabilization of cells, 0.4µg/mL digitonin was added to cell
569 suspensions in the respiratory chamber. Permeabilized cells were then energized with either
570 ETC-I-I (5mM malate, 2.5mM glutamate) or ETC-II (5mM succinate) substrates. In the case
571 of permeabilized cells energized with succinate, 1µM rotenone (ETC-I inhibitor) was added to
572 evaluate the OCR downstream of complex I. In permeabilized cells, ADP-phosphorylation and
573 resting states were stimulated by the direct addition of 5mM ADP and 1µM oligomycin (ATP
574 synthase inhibitor), respectively, onto the respiratory chamber. Both intact and permeabilized
575 cells were titrated with MS-L6 through direct injection of MS-L6 onto the chamber using a
576 Hamilton syringe.

577 *Measurement of OCR of intact mitochondria and mitochondrial fragments*: Intact mitochondria
578 freshly isolated from rat livers (0.5mg/mL) were added to the respiratory chamber containing
579 500µL of mitochondrial assay buffer, 1mM inorganic phosphate, ETC-I substrates (5mM
580 malate, 2.5mM glutamate) and 5mM ADP. The respiratory chamber was then sealed with a
581 cap and titration of the mitochondria with an increasing concentration of MS-L6 was initiated.
582 Regarding the effect of MS-L6 on the OCR of rat liver mitochondrial fragments, mitochondrial
583 fragments (0.5mg/mL) were added to the respiratory chamber containing 500µL of ultrapure
584 water, 5mM inorganic phosphate and ETC-I substrate (1mM NADH). The respiratory chamber
585 was sealed with a cap and titration of mitochondrial fragments with an increasing concentration
586 of MS-L6 was initiated. MS-L6 was always added through direct injection onto the chamber
587 using a Hamilton syringe. The activity of ETC-I, -II and -IV was assessed by measuring the

OCR of 0.5mg/mL mitochondrial fragments suspended in 500µL of water in the presence of 5mM inorganic phosphate that was induced by 1mM NADH, 2mM succinate and 250µM/100µM TMPD/ascorbate, respectively, before and after the addition of 50µM MS-L6. To determine the stability of MS-L6 in medium of cultured cells, 1 x 10^6 of hepatocytes, RL and K422 cells were cultured in 1mL of complete medium in the presence of either DMSO (vehicle control) or 50µM MS-L6 for up to two days. The culture media were collected at different time points of incubation and stored at -80ºC until analysis. The collected culture medium was first placed in the respiratory chamber along with 5mM of inorganic phosphate and 0.5mg/mL of mitochondrial fragments. The respiratory chamber was then sealed, and the OCR of mitochondrial fragments was monitored before and after the injection of 1mM NADH onto the chamber using Hamilton syringe. NADH-driven OCR was determined by subtracting the OCR following NADH addition from OCR before NADH addition. All results were expressed as NADH-driven OCR in the presence of medium collected from 50µM MS-L6-treated cells relative to that collected from DMSO-treated cells.

Measurement of OCR and ECAR on intact cells using Seahorse technology: Real-time metabolic analysis was performed using the Seahorse Bioscience XFe96 Extracellular Flux Analyzer (Agilent), which allows the simultaneous measurement of cellular oxygen consumption rate (OCR in pmoles/min) and extracellular acidification rate (ECAR in mpH/min). On the day of the assay, 1.5 x 10^5 RL and 2 x 10^5 K422 cells at exponential growth were seeded onto Seahorse 96-well plates coated using Corning Cell-Tak (TMsub), according to the manufacturer's instructions. The number of seeded cells was optimized to ensure 70-80% confluence. Culture medium was replaced by Seahorse XF RPMI assay medium pH 7.4 (Agilent) and the plate was pre-incubated for 30 min at 37°C in a non-CO_2 incubator. Simultaneous OCR and ECAR were then measured using the supplier's instructions under basal conditions (injection of inhibitor diluent *i.e.,* DMSO) and after sequential injections of different inhibitors (MS-L6, Rotenone or IACS-010759). The levels of OCR and ECAR were

normalized against the number of cells per well using the Agilent Seahorse XF imaging and cell counting procedures.

Measurement of glucose and lactate concentrations

The concentrations of glucose and lactate in the culture medium of cultured cells were measured using an automated cell culture analyzer Flex 2 (Nova Biomedical). Initially, 1 x 10^6 hepatocytes, RL and K422 cells were grown in 1mL of complete medium in 12-well plates and were treated with either DMSO (vehicle control) or 50µM MS-L6 for up to 48 h. At 24 and 48 h of culture, cells were counted and centrifuged. Supernatants were collected and kept at -80ºC until analysis by Flex 2. Glucose consumption and lactate production in these cells during the first 24 h of culture were subtracted from the concentrations of glucose and lactate in the culture medium, respectively, and were expressed inµmol per living cell.

Quantification of total cellular adenosine nucleotides

The intracellular levels of adenosine nucleotides (ATP, ADP and AMP) were quantified using high-performance liquid chromatography (HPLC Varian model 410). Initially, 2x 10^6 hepatocytes, RL and K422 cells were grown in 2mL of complete medium in 6-well plates and were then treated with either DMSO (vehicle control) or 50µM MS-L6 for 1 or 2 days. For adenosine nucleotide extraction, cells were first washed with PBS two to three times and then lysed with 500-1000µL of 2.5% PCA (perchloric acid) - 6.25mM EDTA (ethylene diamine tetra acetic acid). The acidic extract was vortexed and then neutralized with 100-200µL of 2N KOH (potassium hydroxide) - 0.3M MOPS. The neutralized solution was centrifuged at 12,000 g for 5 min at 4ºC. The final extract was stored at -80ºC until later analysis by HPLC. For HPLC analysis, 75µL of the final extract was mixed with 35µL of mobile phase and 15µL of 1N HCL, and the mix was vortexed and transferred to HPLC vials. The vials were then placed in the autosampler tray and HPLC runs were initiated (column: Polaris 5 C18-A, mobile phase:

28mM sodium pyrophosphate decahydrate, duration: 30 minutes). HPLC results were delivered as chromatograms showing three peaks (ATP, ADP and AMP) at different retention times. These peaks were integrated and calibrated using HPLC offline software.

Measurement of mitochondrial membrane potential

ΔΨm of mitochondria isolated from rat livers was evaluated with the mitochondrial probe, rhodamine 123 (Thermo Fisher Scientific, R302). The fluorescence of Rhodamine 123 was monitored over time using a PTI Quantamaster C61 spectrofluorometer (excitation: 498nM; emission: 524nM). Briefly, 2mL of buffer containing 5mM inorganic phosphate, 15% BSA, ETC-I substrates (5mM malate, 2.5mM glutamate) and 50nM rhodamine 123 were first added to the cuvette. The resulting basal fluorescence signal was stabilized for approximately one minute. A new steady state directly related to ΔΨm was reached one to two minutes following the addition of 0.5mg/mL of freshly isolated rat liver mitochondria. This was followed by the addition of either 50µM MS-L6 or 1µM rotenone. At the end, 0.875µM FCCP was added to fully depolarize ΔΨm. During the whole experiment, the mix was continuously stirred by means of a magnetic bar. Changes in rhodamine 123 fluorescence were recorded and directly correlated with changes in ΔΨm.

ΔΨm of intact RL and K422 cells was assessed by labelling cells using the two vital mitochondrial probes, tetramethylrhodamine methyl ester TMRM (Thermo Fisher Scientific, I34361) to evaluate ΔΨm and Mito Tracker Green (MTG) to evaluate mitochondrial mass. Cell suspensions were divided into two; the first half was incubated with 200nM TMRM and the second half was incubated with 200nM MTG for 20 min at 37^{o}C. This was followed by treatment of each half with either DMSO (vehicle control), 50µM MS-L6 or 1µM rotenone for another 60 min. The TMRM labelled cell suspension was then further divided into two (one part was treated with CCCP for 5 min) and the fluorescence of TMRM, TMRM + CCCP and

MTG labelled cells was measured using flow cytometry. Results were delivered as TMRM fluorescence (TMRM – TMRM+CCCP) normalized against mitochondrial mass (MTG).

Assessment of "NADH oxidizing" activity of mitochondrial complex I

ETC-I activity (NADH oxidation) of rat liver mitochondrial fragments was assessed spectrophotometrically by following NADH absorbance at 340nM. Briefly, 0.5mg/mL of mitochondrial fragments were first added to 2mL of water containing 10mM inorganic phosphate and 1mM KCN, which blocks electron transfer through mitochondrial complex IV. The recording of NADH absorbance was initiated immediately after the addition of 100µM NADH. This was followed by the addition of 100µM decylubiquinone as the ultimate acceptor of electrons resulting from NADH oxidation by ETC-I. At the end, where indicated, DMSO (vehicle control) or 50µM of MS-L6 was added. The activity of NDI (ETC-I subunit) of yeast mitochondria (*Saccharomyses cerevisiae*) was also assessed in the same way. Yeast mitochondria were a precious gift from Dr. Anne Devin (IBCG CNRS, Bordeaux, France).

Assessment of cellular proliferation

Cellular proliferation was assessed by counting cells using trypan blue. Initially, 1 x 10^6 hepatocytes, RL and K422 cells were seeded in 1mL complete medium in 12-well plates and treated with either DMSO (vehicle control) or 50µM MS-L6 for 48 h. At different time points, 20µL of cell suspension was collected and mixed with 20µL of trypan blue (1:1). Cells were counted using the automated cell counter Luna (Logos Biosystem) and live cell counts were used to construct representative proliferation curves.

Assessment of cell viability

690 Initially, $1x10^5$ of RL and K422 cells were seeded in 100µL complete medium in 96-well plates
691 and treated with either DMSO (vehicle control) or indicated concentrations of MS-L6 or other
692 inhibitors, for 48 h. Cell viability was then assessed either by flow cytometry or by biochemical
693 assays as indicated in the text. In case of flow cytometry analysis, the method of annexin
694 V/propidium iodide double staining was used. Cell suspensions were collected. Pellets were
695 suspended in annexin containing buffer, according to standard protocols. Immediately before
696 analysis, propidium iodide was added to each sample. Flow cytometry data acquisition was
697 carried out using BD LSRFortessa™ or automated Attune™ Flow cytometer (Thermo Fischer
698 Scientific) that analysed all cells in a well, for large scale analysis of hematological cell lines.
699 Data were analyzed using FlowJo software (V10, TreeStar Inc, Ashland, USA). The percentage
700 of the population that was negative for annexin V and propidium iodide labelling was regarded
701 as viable. The same experimental design was used to test MS-L6 effect on the large panel of
702 haematological cell lines. Complementary experiments were performed using the CellTiter-
703 Fluor™ Cell Viability Assay (Promega), which is a non-lytic assay that measures the relative
704 number of viable cells based on cellular protease activity. A similar experimental design was
705 used as that described above to plate cells and administrate treatments, except that endpoint
706 analysis of cell viability was performed using a single-fluorescent reagent that was added in
707 each well after 48 h of treatment, and relative fluorescence was measured using a Fluorimeter
708 plate reader (TECAN) according to the manufacturer's instructions.
709 Finally, the simultaneous determination of live and dead cells by imaging was performed using
710 LIVE/DEAD Viability/Cytotoxicity Assay Kit (L3224 Invitrogen) and is described in the
711 supplementary materials and methods section.
712
713 ***Preclinical evaluation of MS-L6 antitumoral activity in mice models***
714 The ethics committee for animal welfare of the French ministry of higher education and
715 research approved all animal experiments under reference APAFIS#2016083009597532. We

confirm that all experiments were performed according to the relevant guidelines and regulations of this committee.

MS-L6 detection in mice serum: Pre-reglementary determination of the maximal tolerated dose (MTD) of MS-L6 to be used for the preclinical evaluation of its antitumoral efficacy was first performed. During these experiments, submandibular blood samples were collected 1 h after intraperitoneal injections of 10 to 50mg/kg of MS-L6. Plasma was stored at -20°C until analysis. The chromatographic system used for MS-L6 quantification consisted of an Ultimate 3000 system coupled with MS/HRMS Q-Exactive Plus Orbitrap mass spectrometer (Thermo Scientific, Germany) equipped with electrospray ionization source (LC-MS/HRMS). The detailed protocol is described in the supplementary materials and methods section.

Evaluation of MS-L6 antitumoral efficacy in cell lines-derived xenografts models: The experiments were performed by ANTINEO (Lyon, France), a CRO specialized in preclinical oncology. The detailed protocol is described in the supplementary materials and methods section. Briefly, 5 x 10^6 RL or SUDHL4 cells were first subcutaneously injected into SCID mice per injection. Mice were randomized when tumors reached a mean volume of 100mM^3 for the 2 groups (control and MS-L6). Tumor volume was measured three times a week. MS-L6 was administered by intraperitoneal injection five times a week, at a dose of 50mg/kg. Control diluent (DMSO) was also administered by intraperitoneal injection five times a week.

FIGURE LEGENDS

<u>Figure 1:</u> MS-L6 inhibits respiration of hepatocytes and cancer cells through ETC-I.

*Panel (**A**)* reports OCR of intact hepatocytes, RL and K422 cells as function of MS-L6 concentration. The respective IC_{50} values of MS-L6 were calculated by fitting of dose response curves in Graphpad Prism and indicated above each trace. Data are shown as means ± SD, n=3.

*Panels (**B** and **C**)* report OCR of digitonin permeabilized hepatocytes, RL and K422 cells treated with the indicated concentrations of MS-L6, driven by ETC-I (Glut/Mal :5mM malate, 2.5mM glutamate) or ETC-II (Succ/Rot:5mM succinate, 1µM rotenone) substrates in mitochondrial assay buffer, under ADP phosphorylating conditions (5mM ADP) and resting state (1µM oligomycin), respectively. Data are shown as means ± SD, n=3. *Panel (**D**)* reports OCR of 0.5mg/mL of intact rat liver mitochondria driven by ETC-I substrate (Glut/Mal) as function of MS-L6 concentration under phosphorylating conditions. Data are shown as means ± SD, n=3. *Panel (**E**)* reports OCR of 0.5mg/mL of rat liver mitochondrial fragments driven by ETC-I substrate (1mM NADH, in the presence of 5mM inorganic phosphate) as function of MS-L6 concentration. Data are shown as means ± SD, n=3. *Panel (**F**)* reports OCR of 0.5mg/mL of rat liver mitochondrial fragments driven by the substrates of ETC-I (1mM NADH), ETC-II (2mM succinate) and ETC-IV (250µM/ 100µM TMPD/Ascorbate), respectively, in the presence of DMSO (vehicle control) or 50µM MS-L6. Data are shown as means ± SD, n=3. *Panel (**G**)* reports ETC-I activity measured by following NADH absorbance spectrophotometrically at 340nM of rat liver mitochondrial fragments in the presence of DMSO (vehicle control) or 50µM MS-L6. First, mitochondrial fragments were incubated with 100µM NADH in the presence of 1mM KCN, and then 100µM decylubiquinone was added. Where indicated, DMSO (black trace) or 50µM MS-L6 (pink trace) was added. The absorbance curves represent one typical experiment; similar results were obtained in two others. *Panel (**H**)* reports OCR of 0.5mg/mL mitochondrial fragments, incubated with DMSO (vehicle control) or 50µM MS-L6, upon titration with increasing concentrations of ETC-I substrate, NADH. Maximal velocity (Vmax) and Michaelis constant (Km) of each trace are indicated. Data are shown as means ± SD, n=3.

Figure 2: MS-L6 drops ΔΨm in rat liver mitochondria and cancer cells.

*Panels (**A-C**)* report ΔΨm of 0.5mg/mL of intact rat liver mitochondria energized with ETC-I substrate (Glut/Mal), with ETC-II substrate (Succ), or with ETC-I substrate (Glut/Mal) after cyclosporine A (CsA) pretreatment, respectively, upon treatment with either 1µM rotenone (blue curve) or 50µM MS-L6 (pink curve). At the end, 0.875µM FCCP was added to fully depolarize ΔΨm. *Panels (**D and F**)* report ΔΨm of 0.5mg/ml of intact rat liver mitochondria energized with Glut/Mal, upon treatment with 50µM MS-L6 or 0.875µM FCCP followed by addition of ATP, or with 50µM MS-L6 followed by addition of ATP plus oligomycin, respectively. All curves illustrate one typical experiment and similar results were obtained in 2 others. *Panel (**F**)* reports ΔΨm of intact RL and K422 cells, measured 1h post-treatment with DMSO (vehicle control), or different combinations of 50µM MS-L6, 1µM rotenone and 2µg/mL oligomycin. Data are shown as means ± SD, n=3.

Figure 3: MS-L6 modifies the energy status in cancer cells.

*Panel (**A**)* represents typical HPLC chromatograms showing the peaks of ATP, ADP and AMP of entire hepatocytes, RL and K422 cells that were cultured in the presence of DMSO (vehicle control) or 50µM MS-L6 up to 3h. *Panel (**B**)* represents calculated ATP/ADP ratios obtained after 3, 24 and 48h of treatment. Data are shown as means ± SD, n=3. *Panel (**C**)* reports OCR of rat liver mitochondrial fragments driven by ETC-I substrate (1mM NADH) in the presence of culture medium collected from hepatocytes, RL and K422 cells at different time points post-treatment with 50µM MS-L6 relative to culture medium from control cells (% of control). Data are shown as means ± SD, n=3.

Figure 4: MS-L6 induces metabolic shift towards aerobic glycolysis in cancer cells.

*Panel (**A**)* reports glucose consumption and lactate production in hepatocytes, RL and K422 cells that were cultured in the presence of either DMSO (vehicle control) or 50µM MS-L6 for 48h. Metabolic fluxes are expressed as number of units (µmol) per unit of living cells per 24h.

The mean is indicated, n=3. *Panel (**B**)* reports real time OCR and ECAR measured using seahorse technology in RL and K422 cells treated with increasing final concentrations of MS-L6 (0.65µM to 5µM), IACS-010759 (0.65µM to 5µM) or rotenone (0.65 to 5nM). The arrows indicate the progressive injection of the inhibitors to obtain the final concentration indicated for MS-L6 and IACS-01075. The final concentration is 10x lower for rotenone. Data are shown as means ± SD, n=3.

Figure 5: MS-L6 reduces proliferation of cancer cells lines in vitro.

*Panel (**A**)* reports cellular proliferation in real time of hepatocytes, RL and K422 cells treated with DMSO (vehicle control) or 50µM MS-L6. Initially, 1 x 10^6 cells were seeded, and cells were then counted at different time points of incubation. Data are shown as means ± SD, n=3. *Panels (**B, C**)* report data obtained in one representative experiment of flow cytometry analysis after annexin V/PI double staining. Analysis was performed 48h after treatment of RL, K422 and SUDHL4 cells with DMSO diluent (NT), 10µM MS-L6, 10µM IACS-0105-759 or 1µM rotenone. *Panel (**B**)* reports the number of live cells: automated flow cytometry analysis allows total and live cells count per well. To standardise the analyses between cell lines and experiments, the mean number of live cells in replicate wells treated with the diluent (NT) was calculated and then the % of live cells relative to this mean was calculated. Each point represents the result obtained for a replicate well. Mean is indicated. *Panel (**C**)* represents a typical flow cytometry contour plots obtained in parallel after annexin V/PI double staining analysis (X axis: Annexin, Y axis: PI) in one replicate well. The histograms represent quantification of these analyses, shown as the percentage of cells in the different apoptosis stages in all well replicates. Data are shown as mean ± SD, n>6. *Panel (**D**)* reports the percentage of viable cells detected 48h post-treatment with 10µM MS-L6 or IACS-010759 in a series of haematological cell lines. The % of viable cells treated with MS-L6/IACS-010759

compared to cells treated with diluent is indicated, calculated as in *panel (**B**)*. Data are shown as means ±SD of 2 or 3 independent experiments including at least 4 replicates.

Figure 6: Yeast NDI-1 complementation decreases MS-L6 toxicity on tumoral cell.

*Panel (**A**)* reports MS-L6 effect on NADH oxidation activity (as used in the Fig.1G) of yeast mitochondria. NADH absorbance was measured spectrophotometrically at 340nM. NDI-1 was functionally isolated from the remaining part of the MRC by incubating yeast mitochondria with 100µM NADH substrate, 1mM KCN to block electron transfer through complex IV and 100µM decylubiquinone as an ultimate accepter of electrons. Then, where indicated, DMSO (black trace) or 50µM MS-L6 (pink trace) was added. These curves represent one typical experiment; similar results were obtained in two others. *Panel (**B**)* reports the viability of K422 overexpressing (NDI-I) or not (CT) yeast NDI-1 protein, following treatment with increasing dose of MS-L6, IACS-010759 or Rotenone. Results are expressed as the percentage of cell treated with the vehicle (DMSO). Viable cells were detected using CellTiter-Fluor™ Cell Viability Assay. Each point represents the mean of 4 experimental replicates and 4 independent experiments were analysed.

Figure 7: MS-L6 displays antitumoral activity in preclinical models.

*Panel (**A**)* reports (left) MS-L6 dosage in the sera of mice during the pilot preliminary toxicity experiments using LC/MS analysis, 1h after IP injection of increasing doses of the molecule and (right) the short procedure used for preclinical evaluation of MS-L6 effect. After xenograft of human lymphoma cell lines in SCID mice, animals with nascent tumours were treated with diluent (DMSO) or 50mg/kg MS-L6 by IP injection, 5/7 days per week, until the maximal ethically accepted volume was reached. *Panel (**B**)* reports tumour volume evolution following treatment of mice subcutaneous xenografts of RL (left) and SUDHL4 (right) cells, after treatment with MS-L6 or diluent (untreated).

Figure S1: Schematic diagram of the OXPHOS machinery and inhibitors.

This figure reports the main chemical steps of OXPHOS, including the four protein complexes of the electron transport chain (ETC) and ATP synthase, with classical substrates and inhibitors used in the experiments. Briefly, the respiratory chain can be fed by electrons coming from NADH (equivalent to Glutamate/Malate), succinate or TMPD/Ascorbate (artificial electron donor) through ETC-I, ETC-II and ETC-IV, respectively. These electrons are then transferred to ETC-IV where they are accepted by O_2, the ultimate electron acceptor. The forward electron flux through the ETC drives proton pumping, resulting in a proton gradient across the IMM. Finally, ATP synthase exploits the energy of this gradient to drive the phosphorylation of ADP into ATP.

Figure S2: MS-L6 induces death of cancer cells.

*Panel (**A**)* reports the percentage of viability of hepatocytes 24 and 48h post-treatment with either DMSO (vehicle control) or 50µM MS-L6. Initially, 1 x 10^6 hepatocytes were seeded and were then counted at 24 and 48h of incubation. Data are shown as means ± SD, n=3. *Panel (**B**)* reports LDH activity measured in culture medium collected from hepatocytes treated with 50µM MS-L6 relative to control cells at 24 and 48h of incubation. Data are shown as means ± SD, n=3. *Panel (**C**)* represents typical flow cytometry dot plots of RL and K422 cells co-labelled with Annexin V and PI and treated as indicated. Histograms below represent the percentage of viability of RL and K422 cells 24 and 48h post-treatment with either DMSO or 50µM MS-L6. Data are shown as means ± SD.

Figure S3: MS-L6 reduces living cell number of cancer cells.

*Panel (**A**)* reports IC_{50} values obtained 48h post-treatment over a large concentration range (10^{-7} to 10^{-4}M) of MS-L6 using 19 haematological cell lines. The CellTiter-Fluor™ Cell Viability Assay was used to detect viable cells. The top left panel shows typical IC_{50} curves obtained on RL and K422 cells 48h post treatment treated using a large concentration range

(10^{-7} to 10^{-4}M) of MS-L6, with the logarithm of MS-L6 concentration in X and the biochemical measure of cell viability value in Y. GraphPad Prism algorithm was used to drive the curves and calculate IC_{50} values reported in the right table. Each point in the IC_{50} curve represents the mean of 15 well replicates. IC_{50} values in the right table represent the mean of the 3 points values (independent experiments) in these IC_{50} curves. The bottom left panel shows images obtained 48h post-treatment of RL and K422 cells with or without 50µM (5.10^{-5}M) of MS-L6 in one respective replicate well of RL or K422 cells. Same experimental analysis was used for all the cell lines analysed, and respective IC_{50} values are reported in the right table. *Panel (**B**)* reports the viable cell number 48h post-treatment with 10 and 25µM MS-L6, IACS-010759 or IM-156 (ETC-1 inhibitor in clinical trial) using the CellTiter-Fluor™ Cell Viability Assay in two rhabdomyosarcoma cell lines. Each individual value represents the mean of 4 replicates. The median is indicated, n=4.

Figure S4: High concentration of MS-L6 induces death of lymphoma and pediatric sarcoma cancer cells.

Live/dead cell analysis of B lymphoma (RL and K422) and rhabdomyosarcoma (RH30) cells treated with 10µM and 50µM MS-L6. Treatment with 10µM gambogic acid was used as an inducer of cell death. Images observed 48h post-treatment are shown: bright field (a), green filter to detect labelling of viable cells (b), red filter to detect labelling of dead cells, and merge images to detect both (d).

Figure S6: NDI1 complementation experiments

*Panel (**A**)* depicts maps of lentiviral vectors used to express yeast NDI1 protein and its corresponding control vector. *Panel (**B**)* reports NDI1 lentiviral vector expression in green and control vector expression in red following infection of K422 cells. *Panel (**C**)* reports NDI1

895 expression measured by RT-qPCR, in CT and NDI1 K422 infected cells. NDI1 DNA template
896 was used as the positive control.
897
898

SUPPLEMENTARY MATERIAL& METHODS

IC_{50} value determination

The day before treatments, RL and Karpas cells (7500 and 15000 cells respectively) were seeded in 25µL/well of RPMI (1% Penicillin-streptomycin, 10% SVF), in one black 384-well plate with transparent bottom (Greiner, order no. 781091). MS-L6 partitioning was performed using TECAN HP D300 dispenser, 15 replicates per conditions and normalization with 0.5% final DMSO. After 48h of treatment 25µL/well of Cell-titer fluor Assay (Promega, reference G6082) reagent was dispensed, and read fluorescence on TECAN Infinite F500 reader (ex 380-400nm / em 505nm) following manufacturer instructions. GraphPad Prism software was used to fit dose response curves to determine the IC_{50} values. The X values are logarithms of concentrations. Y value is biochemical measurement of live cell number. IC_{50} (inhibitory concentration) curves are dose response curves used to determine the specific drug concentration (IC_{50} value) required to reduce of the population of viable cells by 50% when compared to cells grown with no exposure to the drug.

Live/dead cells analysis

The day before treatments, cells were seeded in 80µL/well of RPMI (1% Penicillin-streptomycin, 10% SVF), in one 96-well plate with transparent bottom. Treatments were added the next day in 20µL/well with the appropriate dilution to obtain the final working concentration of each compound. After 48h of treatment, the simultaneous determination of live and dead cells by imaging was performed using LIVE/DEAD Viability/Cytotoxicity Assay Kit (L3224 Invitrogen) according to supplier protocol. This two-colour fluorescence cell viability assay is based on the simultaneous detection of live and dead cells with two probes that recognize parameters of cell viability – intracellular esterase activity with green

fluorescence in live cells (ex/em ~495nM/~515nM) and plasma membrane integrity – DNA with red fluorescence in dead cells (ex/em ~495nM/~635nM). Briefly, 100µl/well of a 2x working solution of 2µM calcein AM and 4µM EthD-1 was added following manufacturer instructions, and images were acquired using EVOS® FL Imaging System (Life Technology).

Quantification of MS-L6 in sera of mice:

The chromatographic system used for MS-L6 quantification consisted of an Ultimate 3000 system coupled with MS/HRMS Q-Exactive Plus Orbitrap mass spectrometer (Thermo Scientific, Germany) equipped with electrospray ionization source (LC-MS/HRMS). Chromatographic separation was achieved on an Atlantis-Hilic chromatographic column (150 × 2.1mM, 3µm) (Waters, USA) using a gradient elution program. The mobile phase consisted to water, acetonitrile and acetate buffer (100mM, pH 5.0). Data acquisition was performed using Full scan mode with mass resolution set at 70,000 FWHM. Analysis was performed in the positive ion mode and L6 and internal standard (I.S.) ions $[M+H]^+$ were monitored at m/z 387.16743 and 373.15168, respectively. Samples were prepared by protein precipitation. 10µL of I.S. (1µg/mL) was added to 50µL of plasma, before introducing then 300µL of acetonitrile. Samples were vortexed for 30 s, and centrifuged at 13,000 g for 10 min. The clear supernatant was then transferred to a glass vial, evaporated under a slight nitrogen stream at 37°C. Finally, the residue was reconstituted in 100µL of mobile phase and 10µL were injected in LC-MS/HRMS.

Evaluation of MS-L6 antitumoral efficacy in cell lines-derived xenografts models:

The experiments were performed by ANTINEO (Lyon, France), a CRO specialized in preclinical oncology. Briefly, 5 x 10^6 RL or SUDHL4 cells were first subcutaneously injected into SCID mice per injection (200 µL). To bypass the heterogeneity of tumor growth, 2 x 2mM pieces of a first tumor were then surgically implanted into the flanks of other animals. This set

of mice was used for the efficacy study. Mice were randomized when tumors reached a mean volume of 100mM^3 for the 2 groups (control and L6). All mice were observed to detect any toxic effects of the product. The endpoints are defined by animal ethics as a tumor diameter of > 18mm, significant weight loss or alteration of animal well-being. To assess the effectiveness of the compounds on tumorigenesis, tumor volume was measured three times a week. The sizes of the primary tumors were measured using calipers and the tumor volume (TV) was extrapolated to a sphere using the formula TV= 4/3 π x r3, by calculating the mean radius from the two measurements. The median and standard deviation were also calculated for each group. Median is preferred to mean to exclude extreme values. L6 were administered by intraperitoneal injection five times a week, at a dose of 50mg/kg. Control DMSO was also administered by intraperitoneal injection five times a week.

Figures

Figure 1

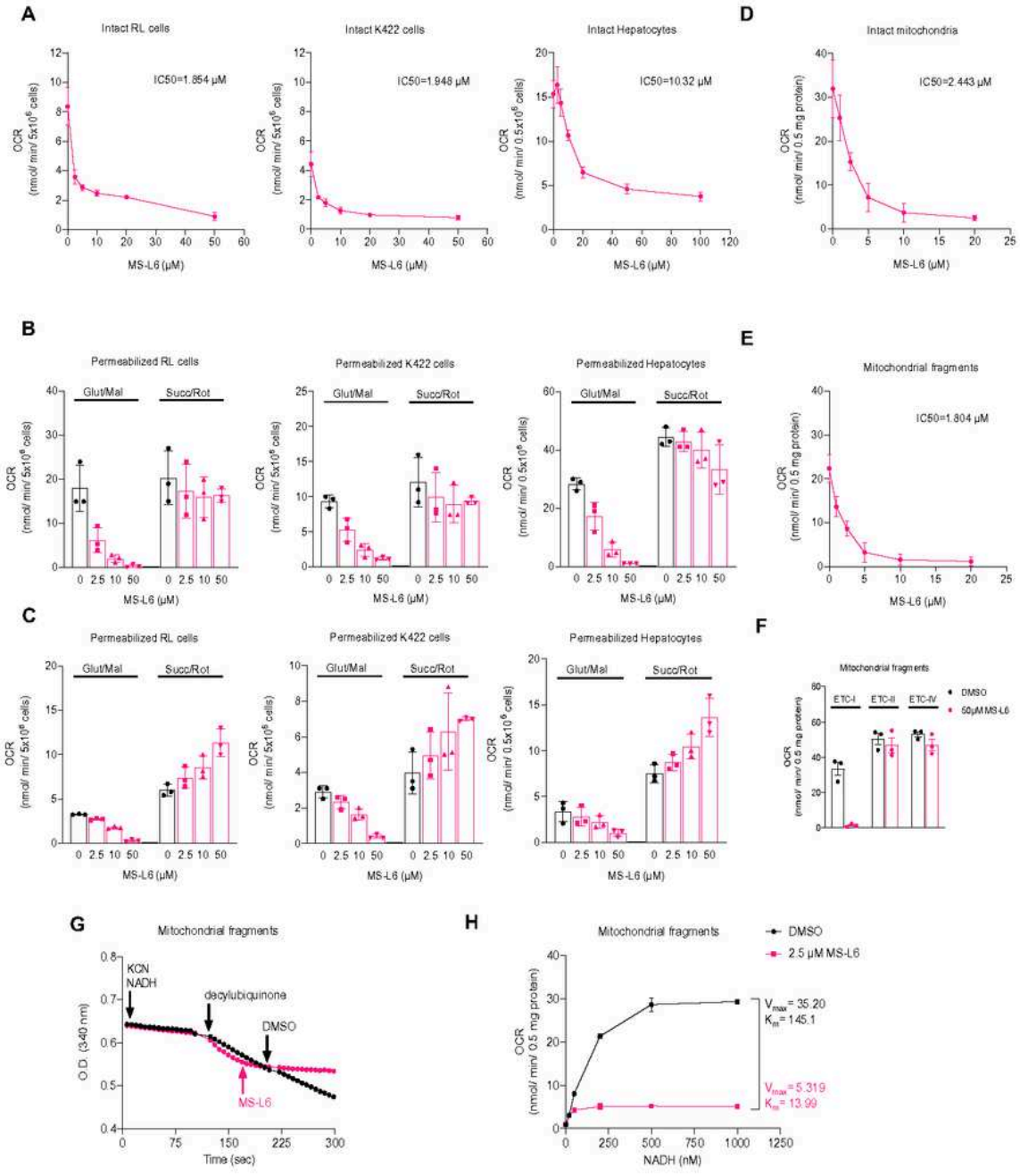

Figure 1

MS-L6 inhibits respiration of hepatocytes and cancer cells through ETC-I.

Panel (A) reports OCR of intact hepatocytes, RL and K422 cells as function of MS-L6 concentration. The respective IC50 values of MS-L6 were calculated by fitting of dose response curves in Graphpad Prism and indicated above each trace. Data are shown as means ± SD, n=3.

Panels (B and C) report OCR of digitonin permeabilized hepatocytes, RL and K422 cells treated with the indicated concentrations of MS-L6, driven by ETC-I (Glut/Mal :5mM malate, 2.5mM glutamate) or ETC-II (Succ/Rot:5mM succinate, 1μM rotenone) substrates in mitochondrial assay buffer, under ADP phosphorylating conditions (5mM ADP) and resting state (1μM oligomycin), respectively. Data are shown as means ± SD, n=3. Panel (D) reports OCR of 0.5mg/mL of intact rat liver mitochondria driven by ETC-I substrate (Glut/Mal) as function of MS-L6 concentration under phosphorylating conditions. Data are shown as means ± SD, n=3. Panel (E) reports OCR of 0.5mg/mL of rat liver mitochondrial fragments driven by ETC-I substrate (1mM NADH, in the presence of 5mM inorganic phosphate) as function of MS-L6 concentration. Data are shown as means ± SD, n=3. Panel (F) reports OCR of 0.5mg/mL of rat liver mitochondrial fragments driven by the substrates of ETC-I (1mM NADH), ETC-II (2mM succinate) and ETC-IV (250μM/ 100μM TMPD/Ascorbate), respectively, in the presence of DMSO (vehicle control) or 50μM MS-L6. Data are shown as means ± SD, n=3. Panel (G) reports ETC-I activity measured by following NADH absorbance spectrophotometrically at 340nM of rat liver mitochondrial fragments in the presence of DMSO (vehicle control) or 50μM MS-L6. First, mitochondrial fragments were incubated with 100μM NADH in the presence of 1mM KCN, and then 100μM decylubiquinone was added. Where indicated, DMSO (black trace) or 50μM MS-L6 (pink trace) was added. The absorbance curves represent one typical experiment; similar results were obtained in two others. Panel (H) reports OCR of 0.5mg/mL mitochondrial fragments, incubated with DMSO (vehicle control) or 50μM MS-L6, upon titration with increasing concentrations of ETC-I substrate, NADH. Maximal velocity (Vmax) and Michaelis constant (Km) of each trace are indicated. Data are shown as means ± SD, n=3.

Figure 2

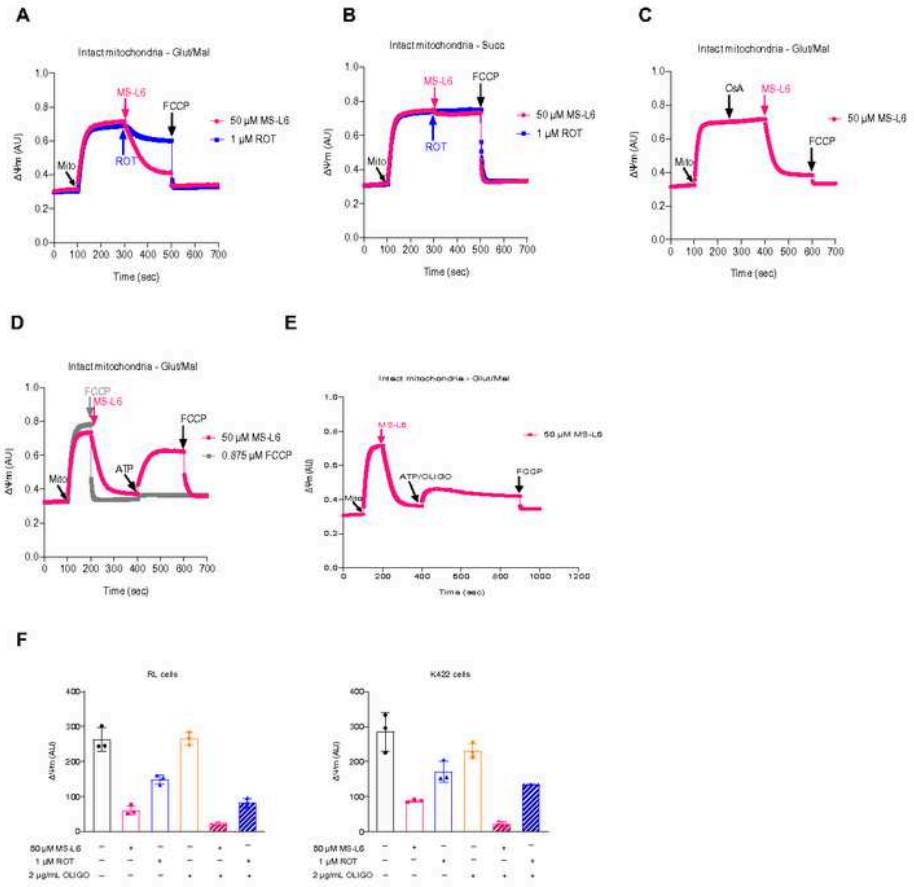

Figure 2

MS-L6 drops ΔΨm in rat liver mitochondria and cancer cells.

Panels (A-C) report ΔΨm of 0.5mg/mL of intact rat liver mitochondria energized with ETC-I substrate (Glut/Mal), with ETC-II substrate (Succ), or with ETC-I substrate (Glut/Mal) after cyclosporine A (CsA) pretreatment, respectively, upon treatment with either 1µM rotenone (blue curve) or 50µM MS-L6 (pink

curve). At the end, 0.875μM FCCP was added to fully depolarize ΔΨm. Panels (D and F) report ΔΨm of 0.5mg/ml of intact rat liver mitochondria energized with Glut/Mal, upon treatment with 50μM MS-L6 or 0.875μM FCCP followed by addition of ATP, or with 50μM MS-L6 followed by addition of ATP plus oligomycin, respectively. All curves illustrate one typical experiment and similar results were obtained in 2 others. Panel (F) reports ΔΨm of intact RL and K422 cells, measured 1h post-treatment with DMSO (vehicle control), or different combinations of 50μM MS-L6, 1μM rotenone and 2μg/mL oligomycin. Data are shown as means ± SD, n=3.

Figure 3

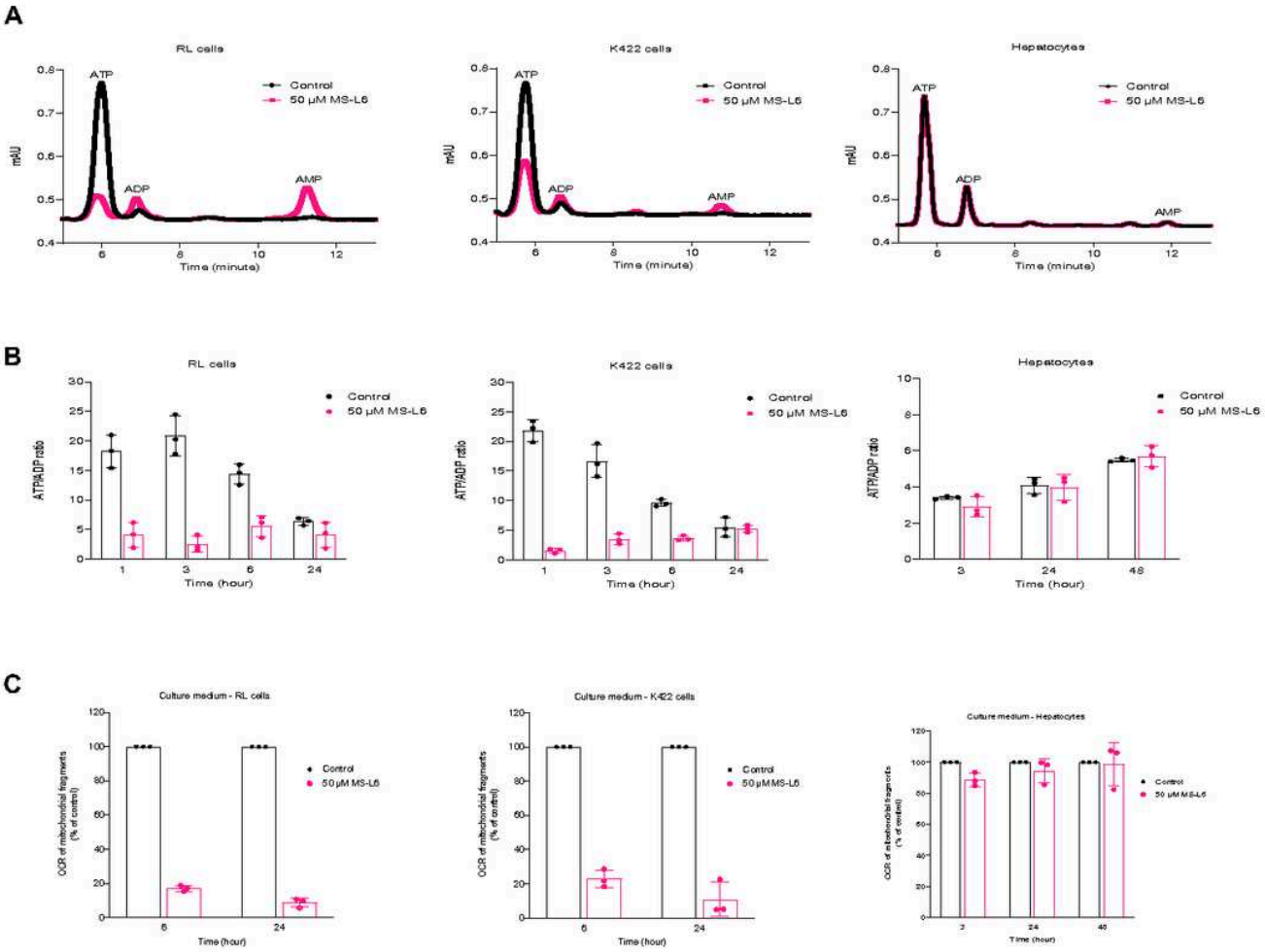

Figure 3

MS-L6 modifies the energy status in cancer cells.

Panel (A) represents typical HPLC chromatograms showing the peaks of ATP, ADP and AMP of entire hepatocytes, RL and K422 cells that were cultured in the presence of DMSO (vehicle control) or 50µM MS-L6 up to 3h. Panel (B) represents calculated ATP/ADP ratios obtained after 3, 24 and 48h of treatment. Data are shown as means ± SD, n=3. Panel (C) reports OCR of rat liver mitochondrial fragments driven by ETC-I substrate (1mM NADH) in the presence of culture medium collected from hepatocytes, RL and K422 cells at different time points post-treatment with 50µM MS-L6 relative to culture medium from control cells (% of control). Data are shown as means ± SD, n=3.

Figure 4

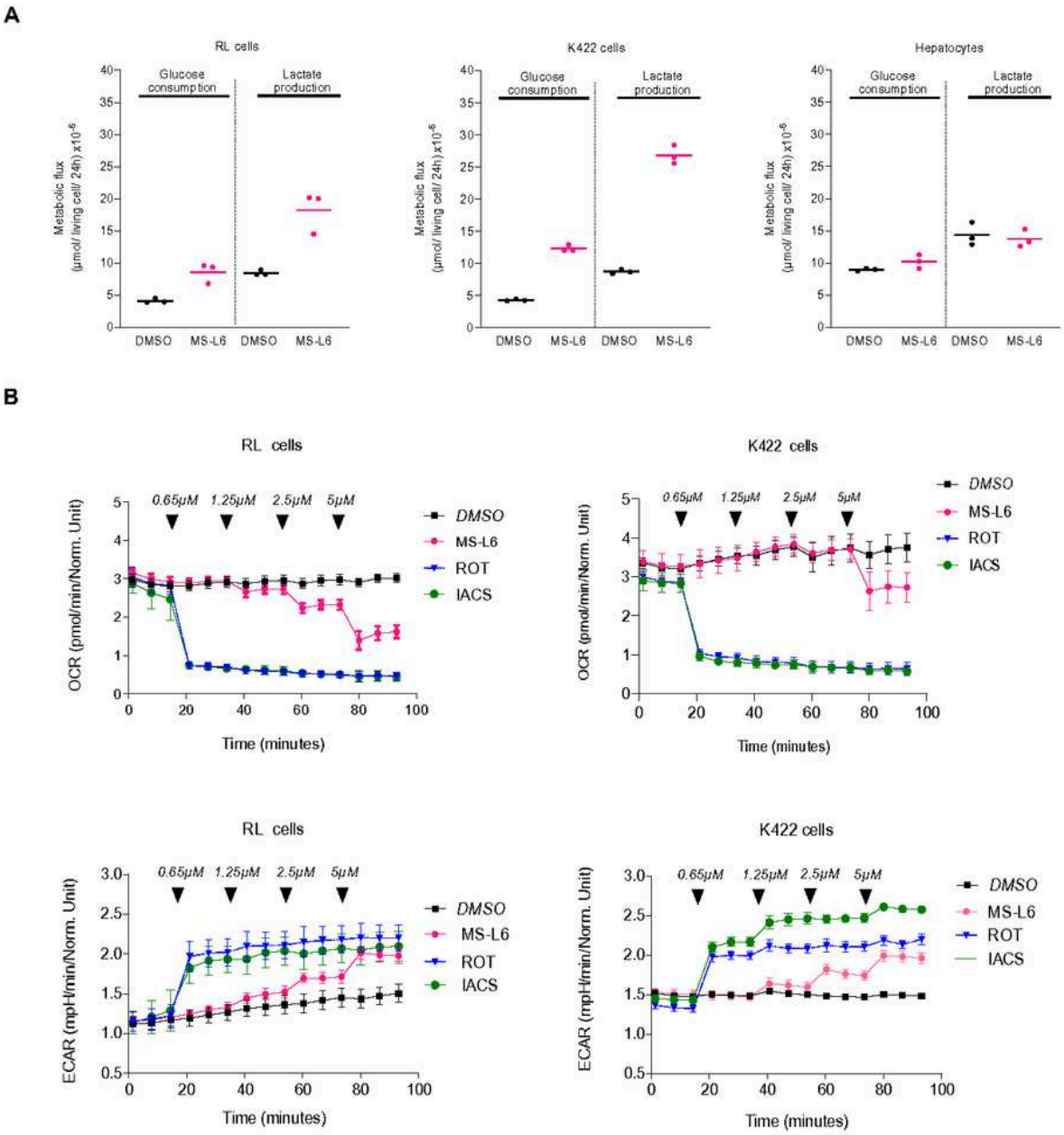

Figure 4

MS-L6 induces metabolic shift towards aerobic glycolysis in cancer cells.

Panel (A) reports glucose consumption and lactate production in hepatocytes, RL and K422 cells that were cultured in the presence of either DMSO (vehicle control) or 50μM MS-L6 for 48h. Metabolic fluxes are expressed as number of units (μmol) per unit of living cells per 24h.

The mean is indicated, n=3. Panel (B) reports real time OCR and ECAR measured using seahorse technology in RL and K422 cells treated with increasing final concentrations of MS- L6 (0.65μM to 5μM), IACS-010759 (0.65μM to 5μM) or rotenone (0.65 to 5nM). The arrows indicate the progressive injection of the inhibitors to obtain the final concentration indicated for MS-L6 and IACS-01075. The final concentration is 10x lower for rotenone. Data are shown as means ± SD, n=3.

Figure 5

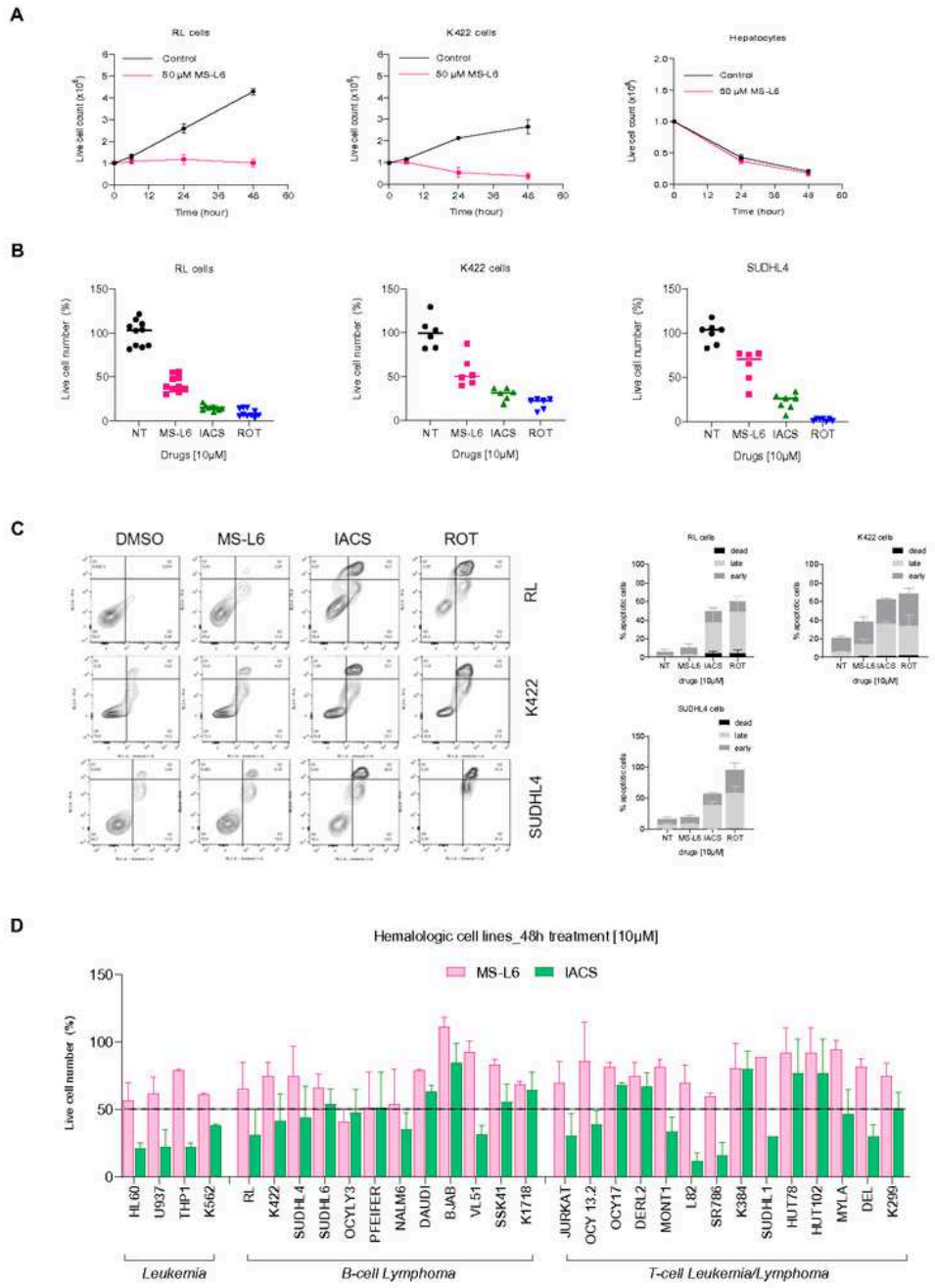

Figure 5

MS-L6 reduces proliferation of cancer cells lines in vitro.

Panel (A) reports cellular proliferation in real time of hepatocytes, RL and K422 cells treated with DMSO (vehicle control) or 50µM MS-L6. Initially, 1 x 106 cells were seeded, and cells were then counted at different time points of incubation. Data are shown as means ± SD, n=3.

Panels (B, C) report data obtained in one representative experiment of flow cytometry analysis after annexin V/PI double staining. Analysis was performed 48h after treatment of RL, K422 and SUDHL4 cells with DMSO diluent (NT), 10μM MS-L6, 10μM IACS-0105-759 or 1μM rotenone. Panel (B) reports the number of live cells: automated flow cytometry analysis allows total and live cells count per well. To standardise the analyses between cell lines and experiments, the mean number of live cells in replicate wells treated with the diluent (NT) was calculated and then the % of live cells relative to this mean was calculated. Each point represents the result obtained for a replicate well. Mean is indicated. Panel (C) represents a typical flow cytometry contour plots obtained in parallel after annexin V/PI double staining analysis (X axis: Annexin, Y axis: PI) in one replicate well. The histograms represent quantification of these analyses, shown as the percentage of cells in the different apoptosis stages in all well replicates. Data are shown as mean ± SD, n>6. Panel (D) reports the percentage of viable cells detected 48h post-treatment with 10μM MS-L6 or IACS-010759 in a series of haematological cell lines. The % of viable cells treated with MS-L6/IACS-010759

compared to cells treated with diluent is indicated, calculated as in panel (B). Data are shown as means ±SD of 2 or 3 independent experiments including at least 4 replicates.

Figure 6

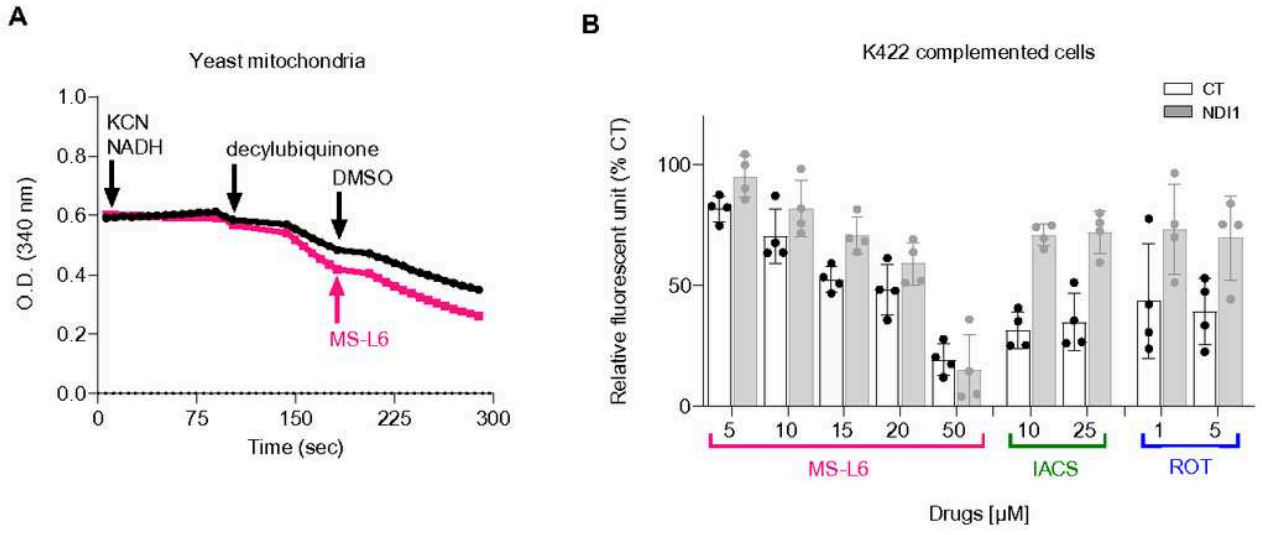

Figure 6

Yeast NDI-1 complementation decreases MS-L6 toxicity on tumoral cell.

Panel (A) reports MS-L6 effect on NADH oxidation activity (as used in the Fig.1G) of yeast mitochondria. NADH absorbance was measured spectrophotometrically at 340nM. NDI-1 was functionally isolated from the remaining part of the MRC by incubating yeast mitochondria with 100µM NADH substrate, 1mM KCN to block electron transfer through complex IV and 100µM decylubiquinone as an ultimate accepter of electrons. Then, where indicated, DMSO (black trace) or 50µM MS-L6 (pink trace) was added. These curves represent one typical experiment; similar results were obtained in two others. Panel (B) reports the viability of K422 overexpressing (NDI-I) or not (CT) yeast NDI-1 protein, following treatment with increasing dose of MS-L6, IACS-010759 or Rotenone. Results are expressed as the percentage of cell treated with the vehicle (DMSO). Viable cells were detected using CellTiter-Fluor™ Cell Viability Assay. Each point represents the mean of 4 experimental replicates and 4 independent experiments were analysed.

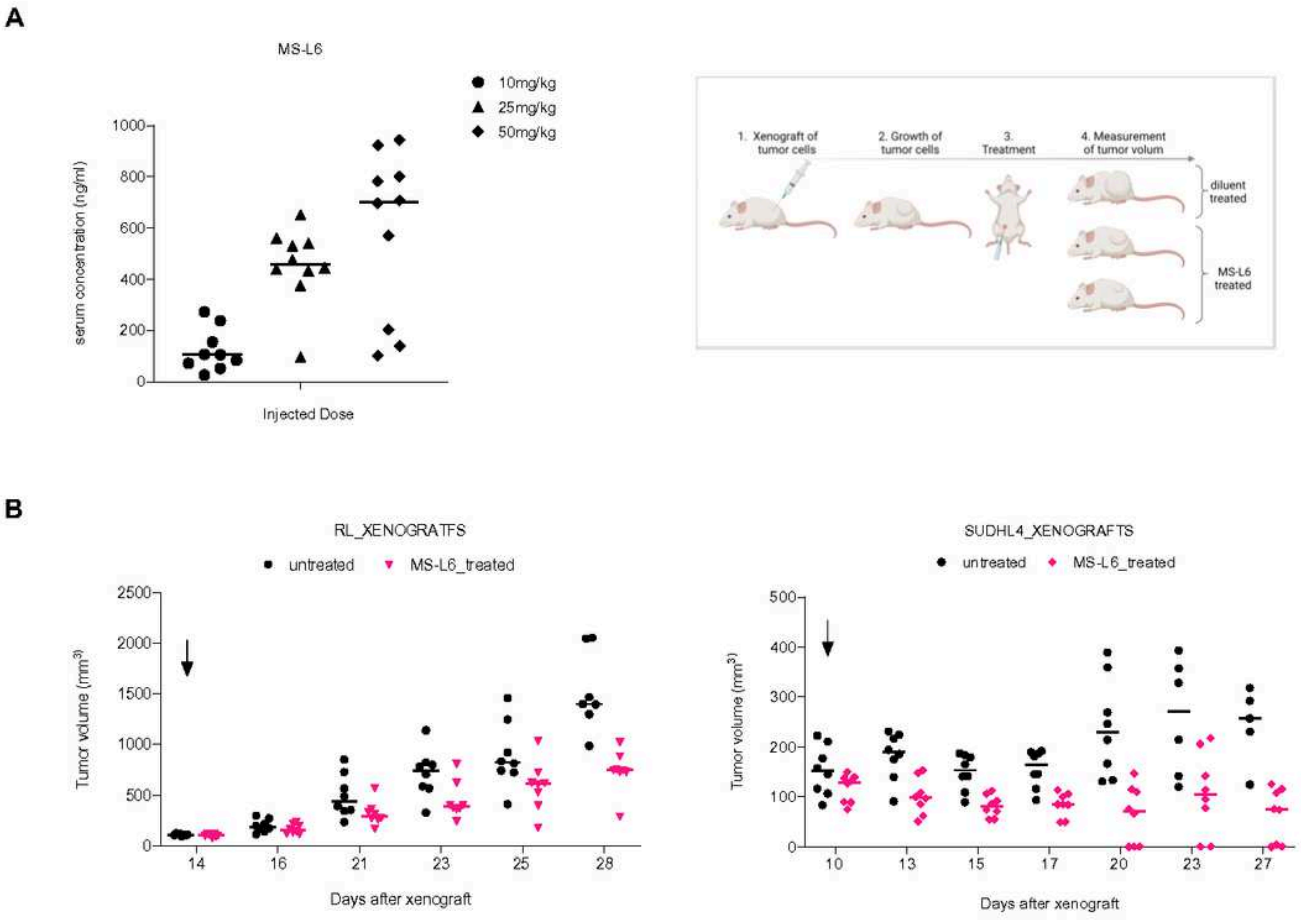

Figure 7

MS-L6 displays antitumoral activity in preclinical models.

Panel (A) reports (left) MS-L6 dosage in the sera of mice during the pilot preliminary toxicity experiments using LC/MS analysis, 1h after IP injection of increasing doses of the molecule and (right) the short procedure used for preclinical evaluation of MS-L6 effect. After xenograft of human lymphoma cell lines in SCID mice, animals with nascent tumours were treated with diluent (DMSO) or 50mg/kg MS-L6 by IP injection, 5/7 days per week, until the maximal ethically accepted volume was reached. Panel (B) reports

tumour volume evolution following treatment of mice subcutaneous xenografts of RL (left) and SUDHL4 (right) cells, after treatment with MS-L6 or diluent (untreated).

Supplementary Files

This is a list of supplementary files associated with this preprint. Click to download.

- 3ComplementaryMaterials.pdf
- 4FinalFigures050720238.png
- 4FinalFigures050720239.png
- 4FinalFigures0507202310.png
- 4FinalFigures0507202311.png
- 4FinalFigures0507202312.png
- 4FinalFigures0507202313.png